



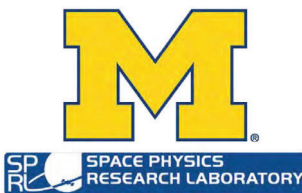
**CYCLONE GLOBAL NAVIGATION
SATELLITE SYSTEM (CYGNSS)**



**Algorithm Theoretical Basis Document
Level 1B DDM Calibration**

UM Doc. No.	148-0137
SwRI Doc. No.	N/A
Revision	Rev 6
Date	8 December 2023
Contract	NNL13AQ00C

Algorithm Theoretical Basis Documents (ATBDs) provide the physical and mathematical descriptions of the algorithms used in the generation of science data products. The ATBDs include a description of variance and uncertainty estimates and considerations of calibration and validation, exception control and diagnostics. Internal and external data flows are also described.





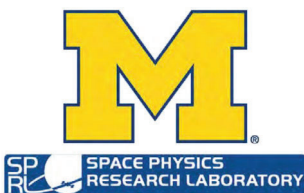
**CYCLONE GLOBAL NAVIGATION
SATELLITE SYSTEM (CYGNSS)**



Algorithm Theoretical Basis Document Level 1B DDM Calibration	UM Doc. No.	148-0137
	SwRI Doc. No.	N/A
	Revision	Rev 6
	Date	8 December 2023
	Contract	NNL13AQ00C

Prepared by: Scott Gleason, Mohammad Al-Khaldi, Darren McKague.

December 2023





Darren S McKague

Approved by:

Darren McKague, CYGNSS UM Project Manager

Date: 12/8/2023

Anthony Russel

Approved by:

Anthony Russel, CYGNSS SOC Manager

Date: 12/8/2023

Chris Ruf

Approved by:

Chris Ruf, CYGNSS Principal Investigator

Date: 12/8/2023





Document Revision History		
Revision	Date	Changes
PRE-RELEASE DRAFT	17 June 2013	N/A
INITIAL RELEASE	14 January 2014	Add unwrapping of the radar range equation to estimate normalized scattering cross-section from received power. Add detailed error analysis.
Rev 1	19 December 2014	Change L1b DDM units to scattering cross-section in meters ² . Add ancillary data product of scattering area in each DDM bin. Add greater detail about algorithm implementation.
Rev 2	20 August 2018	Inclusion of all modifications made to the Level 1A algorithms based on observed on-orbit performance between March 2017 and August 2018.
Rev 3	20 October 2020	Inclusion of all modifications for zenith EIRP calibration.
Rev 4	8 November 2021	Inclusion of nadir and zenith bin ratio corrections, DDMA normalization area re-scaling, NBRCS normalization, and EIRP normalization.
Rev 5	17 October 2023	General reformatting Long duration thermal correction Moved (updated) bin ratio correction to L1A ATBD Merged ocean and land L1 netcdf variables w/ land specular point calculation details Updated nadir antenna pattern rescaling Updated NBRCS rescaling
Rev 6	8 December 2023	Updating L1 uncertainties

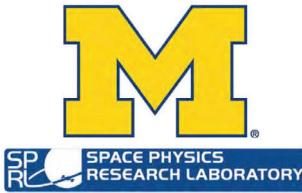


Table of Contents

- I. LEVEL 1B CALIBRATION APPROACH..... 6**
 - A. Forward Model of Scattered Signal Power 6
 - B. Geolocation of Surface Measurement: Solving For The Surface Specular Reflection Point 7
 - C. Mean Sea Surface Height Model..... 7
 - D. Ocean Specular Point Solver Implementation 9
 - E. Level-1B Calibration Algorithm: Watts to σ_0 9
 - F. Expression For Bi-static Radar Cross Section 10
 - G. Calculating Effective and Physical Scattering Areas 11
 - H. Digital to Analog DDM Scaling Issue 12
 - I. Calculating a Normalized Bi-static Radar Cross Section 12
 - J. Altitude Dependent DDMA Area Normalization..... 13
 - K. Characterization of GPS Effective Isotropic Radiated Power (EIRP, v2.1 calibration)..... 14
 - L. Zenith EIRP Calibration (Version 3.0 calibration) 16
 - M. Rescaling of Nadir Antenna Patterns..... 18
 - N. NBRCS and EIRP Normalization..... 21
- II. CYGNSS LEVEL 1 ERROR ESTIMATION METHOD..... 21**
 - A. Error Analysis Methodology 22
 - B. Rolled Up On-Orbit Level 1 Calibration Errors 22
 - C. Rolled up L1 Uncertainty 23
- III. CONTINUED L1B ALGORITHM UPGRADES 23**
 - A. DDMA normalization area re-scaling 23
 - B. Long Duration Periodic Temperature Correction 25
- IV. MERGER OF OCEAN AND LAND LEVEL 1 NETCDF PRODUCTS..... 29**
 - A. Signal coherency estimator 29
 - B. Additional land L1 parameters..... 32
 - C. Land Specular Point Calculation..... 32
- APPENDIX – LEVEL 1 DATA DICTIONARY 35**



I. LEVEL 1B CALIBRATION APPROACH

This document is the second part of the overall Level 1 Calibration Algorithm Theoretical Basis Document (ATBD) describing the Level 1b calibration. Portions of this ATBD have been re-published in [1, 2].

The Level 1b calibration is performed after the Level 1a calibration and will use external meta-data to convert the Level 1a mapped power in Watts to a delay Doppler map (DDM) of bistatic radar cross section (BRCS) values. This conversion will be done for every pixel in every DDM and requires the following information at the time the science DDM is collected,

- 1) The CYGNSS satellite GPS time, position and velocity in the WGS84 Earth Centered Earth fixed (ECEF) reference frame.
- 2) The GPS satellite position and velocity in the Earth WGS84 Centered Earth fixed (ECEF) reference frame.
- 3) Detailed knowledge of the CYGNSS nadir antenna gain patterns.
- 4) Best estimated attitude knowledge of the CYGNSS spacecraft at the time of the measurement.
- 5) An estimate of the GPS effective isotropic radiative power (EIRP) in the direction of the specular reflection point in the GPS satellite reference frame.

Additional information calculated using the per DDM science meta data and used in the Level 1b calibration of each DDM includes,

- 1) An accurate surface geolocation of the reflection specular point (SP) in the WGS84 ECEF reference frame.
- 2) A precise estimate of the specular reflection point location in the measurement DDM pixel delay and Doppler bins.
- 3) The path length between the GPS satellite and specular reflection point and between the specular reflection point and the CYGNSS spacecraft making the measurement.
- 4) The effective scattering area per DDM bin surrounding the specular point over all delay and Doppler bins.

The above parameters are then used to estimate values of the bistatic radar cross section for each DDM pixel using the forward model described below.

A. Forward Model of Scattered Signal Power

A full expression for the GPS scattered signal power has been previously derived and published in 2000 [3], shown in Equation 1. The original representation has been slightly modified in form and variable names,

$$P_{\hat{\tau},\hat{f}}^g = \frac{P^T \lambda^2}{(4\pi)^3} \iint_A \frac{G_{x,y}^T \sigma_{x,y}^0 G_{x,y}^R}{(R_{x,y}^R)^2 (R_{x,y}^T)^2} \Lambda_{\hat{\tau};x,y}^2 S_{\hat{f};x,y}^2 dx dy \quad (1)$$

where $P_{\hat{\tau},\hat{f}}^g$ is the coherently processed scattered signal power, in Watts. P^T is the GPS satellite transmit power and $G_{x,y}^T$ is the GPS satellite antenna gain. $G_{x,y}^R$ is the CYGNSS satellite receiver antenna gain. $R_{x,y}^T$ and $R_{x,y}^R$ are the transmitter to surface and surface to receiver ranges, respectfully. $\sigma_{x,y}^0$ is the normalized bistatic scattering cross section (NBRCS). λ is the GPS signal carrier wavelength (approx. 19 cm). $\Lambda_{\hat{\tau};x,y}$ is the GPS signal spreading function in delay and $S_{\hat{f};x,y}$ is the frequency response of the GPS signal. A is the surface integration area covering the effective region of diffuse scattering for each delay Doppler bin. The scattered signal power is processed using a 1ms coherent integration intervals over a range of relative delays $\hat{\tau}$ and Doppler frequencies \hat{f} , followed by 1 second of non-coherent averaging. These delay and frequency bins map non-uniquely spatially to physical coordinates on the surface.

The above expression can be simplified using the effective values of several variables across delay and Doppler bins under the integrand of Equation 1. The effective values include the effects of delay and Doppler spreading functions, Λ and S , which have been eliminated from the Equation and are indicated by the over-bar in the following equations. The surface mapping from physical (x, y) coordinates to delay and Doppler coordinates reflects the actual processing as performed in the CYGNSS delay Doppler mapping instrument (DDMI).

$$P_{\hat{\tau},\hat{f}}^g = \frac{P^T \lambda^2 G_{\hat{\tau},\hat{f}}^T \langle \sigma_{\hat{\tau},\hat{f}}^0 \rangle \bar{G}_{\hat{\tau},\hat{f}}^R \bar{A}_{\hat{\tau},\hat{f}}}{(4\pi)^3 (\bar{R}_{\hat{\tau},\hat{f}}^R)^2 (\bar{R}_{\hat{\tau},\hat{f}}^T)^2} \quad (2)$$



where, $\bar{G}_{\hat{\tau}, \hat{f}}^R$ is the effective receiver antenna gain at each delay/Doppler bin. $\bar{R}_{\hat{\tau}, \hat{f}}^T$ and $\bar{R}_{\hat{\tau}, \hat{f}}^R$ are the effective range losses at each delay/Doppler bin and $\bar{A}_{\hat{\tau}, \hat{f}}$ is the effective surface scattering area at each delay/Doppler bin.

All variables in Equation 2 vary with respect to delay $\hat{\tau}$ and Doppler frequencies \hat{f} (which map to the x, y surface grid over the glistening zone), however, for the sake of simplification and with negligible loss in accuracy, several parameters can be estimated and applied as constants across the DDM measurement as expressed below.

B. Geolocation of Surface Measurement: Solving For The Surface Specular Reflection Point

The estimated location of the center of the surface glistening zone of the reflected signal provides the main point of reference for the geo-location of the GNSS-R measurement. This point on the surface is referred to as the specular point and can be estimated mathematically using the physical geometry of the transmitting and receiving satellites and a model of the Earth's ocean surface. The surface specular point estimation algorithm described below is designed for ocean surfaces. The modifications to the specular point estimation algorithm over land is described in detail in Section IV-C.

In the original Level 1 calibration approach, the specular point was solved using a) the position of the receiving satellite, as estimated by the 1Hz single frequency position estimate, b) the estimate of the transmitting satellite using ground based precise ephemeris and c) the WGS84 ellipsoid model of the Earth. This Earth model, although generally accurate enough for most applications, relied on approximations that resulted in residual specular point position estimation errors that were large enough to significantly impact the pixels in the DDM used to calculate the bistatic radar cross section. Subsequently, an improved specular point solver was implemented that used a more accurate DTU10 mean sea surface model [4], combined with a brute force, computationally-efficient specular point solver algorithm.

The specular point on the Earth maps to a single point in the delay-Doppler coordinates in the CYGNSS DDM. The exact specular bin location in the DDM will be located at a fractional pixel location within a single DDM bin. The pixels in the DDM at and surrounding the specular point bin determine the region used to make the surface bistatic radar cross section measurement, the DDM Area (DDMA). The estimation of the DDMA within the Level 1a DDM is described in more detail below using the precise location of the specular point described here. This region of the DDM represents the bins of highest reflected power and smallest spatial footprint on the surface and accurate knowledge of this region is critical for calibration and wind speed retrievals.

The specular point location on the surface can't be reliably estimated using the peak power bin of the DDM. The peak power pixel results from a combination of effects in addition to the specular point location, including thermal noise, speckle noise or asymmetries in the reflected signal waveform (as a result of geometry and antenna pattern non-uniformity). For this reason, the specular point surface location and location of the specular point in the instrument generated DDM is calculated to a sub-pixel level from first principles (i.e. geometry and timing metadata).

C. Mean Sea Surface Height Model

In order to more precisely predict the specular location, it is necessary to account for deviations in the Earth's mean sea surface height as compared to the WGS84 model. For this purpose, we have utilized the DTU10 mean sea surface model [3]. The mean sea surface is the displacement of the sea surface relative to a mathematical model of the Earth and it closely follows the Earth's geoid. The amplitude of the deviation from the WGS84 ellipsoid is generally within approximately ± 100 meters over the Earth's ocean surfaces. The original DTU10 data was reduced to a 1 degree by 1 degree resolution to improve the efficiency of the calculation. Height variations over the same resolution are relatively small. The DTU10 map of sea surface height variations relative to the WGS84 ellipsoid used in the specular point solver is shown in Figure 1.

The path delay error manifests itself as an error in the predicted reflection path delay, which, in turn, becomes an error in the predicted location of the specular bin in the DDM. The error in predicted path delay can be expressed as,

$$\rho = 2 \cos(\theta) \delta h \quad (3)$$

Where ρ is the path delay error, θ is the reflection incidence angle and δh is the relative surface height error with respect to the WGS84 ellipsoid.

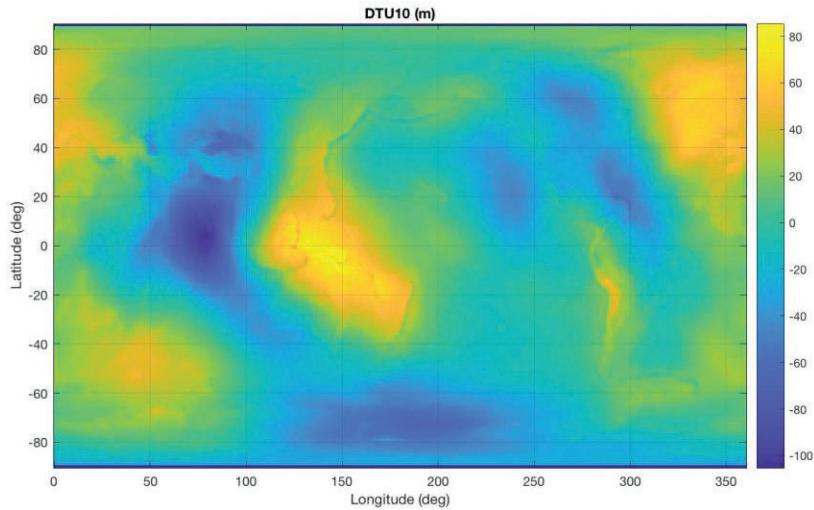


Fig. 1. DTU10 Mean Sea Surface data used for specular point calculation.

The height difference, manifests as a path delay error which becomes an error in the predicted location of the specular bin in the DDM. For a typical incidence angle of 30 degrees, a surface height error of 100 meters could result in 170 meters of path delay error. In the CYGNSS DDM, the delay pixel resolution is approximately 0.25 GPS L1 C/A code chips, and one chip corresponds to approximately 293 meters of delay. Therefore, a 170 m path delay error results in the predicted specular bin in the DDM being offset by 2.25 pixels from where we would expect it on the WGS84 ellipsoid.

Figure 2 shows a plot of specular bin delay difference when using DTU10 as opposed to using WGS84. Specular delay differences are shown for 1 day of measurements for 4 satellites (each shown in 4 separate colors). We can observe that the delay difference (or correction) due to the improved specular point solver varies between -2 and 2.5 pixels in delay space in the DDM. Figure 2 also shows an example measured CYGNSS DDM. In the DDM, the original specular bin solved using WGS 84 model is shown as a red 'X' while the new specular bin solved using DTU10 is shown with a red square. Visually, it is clear the specular bin location calculated with DTU10 is at the correct location in the reflected waveform. Range errors introduced by incorrect specular point prediction primarily impact the L1 calibration due to misidentifying the correct specular point bins (and specular region reflected power) in the DDM measurements. These errors will also degrade the surface vertical ranging accuracy and horizontal geolocation if not corrected.

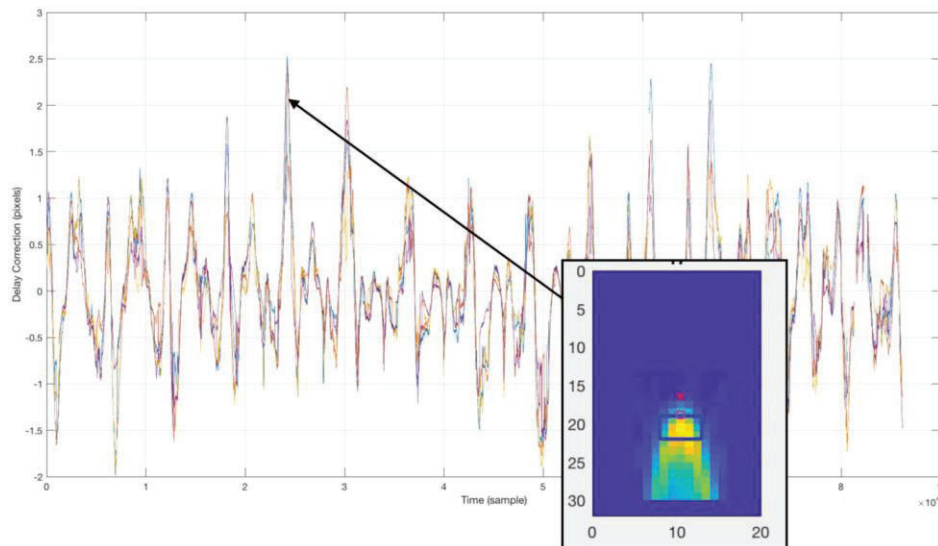


Fig. 2. One day of specular point corrections using the DTU10 model as compared to the WGS84 model. The correction due to the improved specular point solver varies between -2 and 2.5 pixels in delay space in the DDM.



D. Ocean Specular Point Solver Implementation

The new specular point solution is reported in the CYGNSS Level 1 data in the form of the specular point position and velocity variables. It takes approximately 20 seconds to calculate one day of precise specular points within CYGNSS DDMs from one satellite (~320000-640000 DDMs for 1 Hz and 2 Hz data respectively). The algorithm used to solve for ocean specular points is as follows:

- 1) The original specular point solution based on the WGS84 ellipsoid model is used as our initial estimate of the specular point.
- 2) A large 3-D grid of points is constructed around the estimated specular point. This grid has uniform latitude and longitude spacing and is conformal to the WGS84 ellipsoid at each point.
- 3) At each grid point, the DTU10 mean sea surface height is used to shift the altitude. The 1-degree resolution DTU10 data (shown above) is bi-linearly interpolated to find the altitude value at each grid point. The resulting grid is then conformal to the DTU10 surface
- 4) Next, the point in the grid with the minimum reflection path length (from transmitter to the grid point to the receiver) is found. This minimum-path-delay grid point becomes the new specular point location estimate.
- 5) An additional higher resolution grid is constructed around this estimated specular point location and steps 2-4 are repeated several times. In this way, a series of search grids sequentially zoom in on the estimated specular point. The choice of initial grid size and resolution are carefully chosen to prevent erroneous convergence.

The specular point we solve for here is defined as the point on the Earth with the minimum reflection path delay. As the surface what we use is conformal to an arbitrary geoid topology at each grid point, no mathematical constraint is placed on transmitter and receiver incidence angles in this solution. In a strict sense, it is no longer a “specular” point since (if the ocean surface were smooth) a specular reflection would occur at surface locations with equal transmitter and receiver incidence angles, not minimum delay. Nonetheless, the minimum delay point is sufficiently relevant for our purposes since the corresponding specular bin defines the leading edge of the reflected waveform and the specular point represents the center of our iso-delay surface contours within the reflection glistening zone.

E. Level-1B Calibration Algorithm: Watts to σ_0

The Level 1a calibrated DDM represents the received surface signal power in Watts binned over a range of time delays and Doppler frequencies. Before any geophysical parameters can be estimated, these power values must be corrected for non-surface related terms by inverting the forward model shown in Equation 2. The CYGNSS Level 1b calibration generates three data products associated with each Level 1a DDM: 1) A bin by bin calculation of the surface bi-static scattering cross section, σ (not normalized by scattering area), 2) a bin by bin values of the effective scattering areas and 3) a NBRCS value for a DDM Area (DDMA) in a 3 delay x 5 Doppler bin region around the estimated specular point location in the DDM. The first two products will allow users to normalize values of σ to values to σ_0 (scattering cross section per meter squared), over configurable surface extents using summations of the effective scattering areas for individual DDM bins. The values of σ are corrected for the effects of the transmit and receive antennas, range losses and other non-surface related parameters. The effective scattering areas are calculated based on the measurement specific reflection geometry and include the GPS specific delay and Doppler spreading functions. However, care should be taken when using DDM bins away from the specular point, as some of the corrections applied (such as the receive antenna gain and path losses) will degrade at pixels outside the DDMA region. An overview of the CYGNSS Level 1b Calibration is shown in Figure 3.

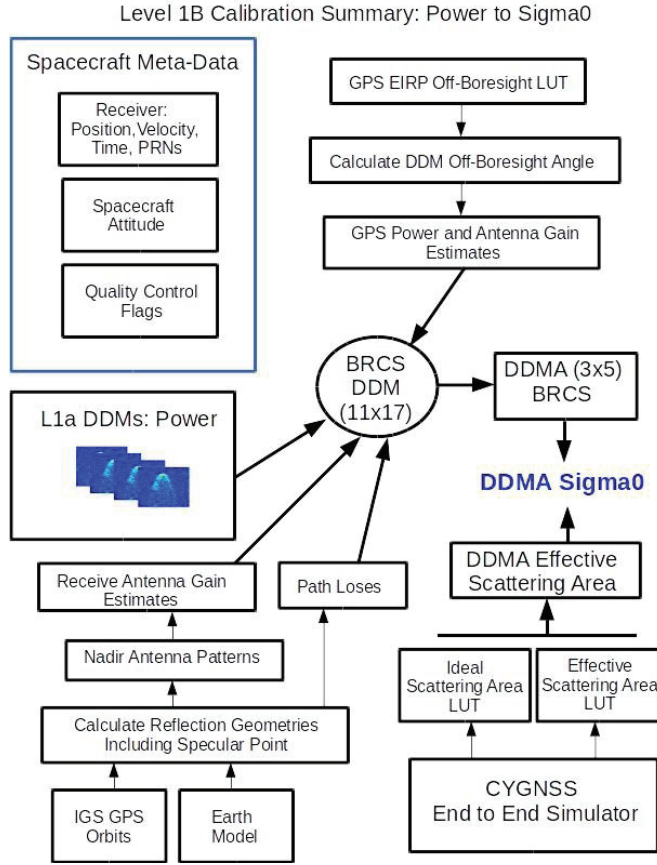


Fig. 3. Overview of CYGNSS Level 1b Calibration.

F. Expression For Bi-static Radar Cross Section

The final expression for the Level 1b DDM can be derived from the expression of the signal forward model, expressed in Equation 2, by solving for the scattering cross section term, σ_0 . As the DDM Level 1b sigma product will not be normalized, we have removed \bar{A} from Equation 2 and replaced the normalized radar cross section σ_0 with a non normalized, σ . Additionally, Receive antenna gain G_{SP}^R , the GPS antenna gain G_{SP}^T , and total path loss (simplified into a single value) R_{SP}^{Total} terms are approximated with their values at the specular point and applied across the whole DDM. The resulting expression for the bin by bin scattering cross section, σ , is,

$$P_{\hat{\tau}, \hat{f}}^{L1b} = \langle \sigma_{\hat{\tau}, \hat{f}}^0 \rangle = \frac{P_{\hat{\tau}, \hat{f}}^g (4\pi)^3}{P^T \lambda^2 G_{SP}^T G_{SP}^R R_{SP}^{Total}} \quad (4)$$

where the individual terms in Equation 4 are as follows,

- 1) $P_{\hat{\tau}, \hat{f}}^g$ is the Level 1a calibrated signal power at a specific delay ($\hat{\tau}$) and Doppler (\hat{f}) bin.
- 2) R_{SP}^{Total} is the total range loss from the transmitter to the surface and the surface to the receiver at the specular point. When using a relatively small area of the DDM near the specular reflection point, this value can be approximated as the total range from the transmitter to the specular point to the receiver. This term is included in the denominator as it is calculated as a loss $R_{SP}^{Total} = 1/(R_R)^2 \times 1/(R_T)^2$.
- 3) P^T and G^T are the GPS satellite transmit power and antenna gain at the specular point. These values are estimated using a ground based GPS Power Monitor and measurements from the CYGNSS navigation antenna to map the transmit power of individual GPS satellites. Details can be found in [6].
- 4) G_{SP}^R is the receiver antenna gain at the specular point applied across all DDM bins. Applying the SP antenna gain outside the DDMA region will introduce errors that should be accounted for when using pixels outside the DDMA region (3 delay and 5 Doppler around SP).

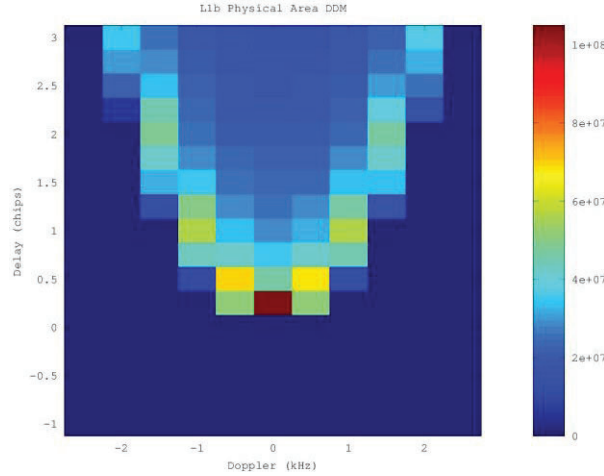


Fig. 4. Physical Scattering Area for a typical DDM reflection geometry. The delays before the specular reflection point do not correspond to any physical region on the surface.

G. Calculating Effective and Physical Scattering Areas

A single delay Doppler bin will contain the captured scattered power across one or more physical regions on the ocean surface. For each delay Doppler bin in the DDM this region will vary both in actual physical size (on the ground surface area) and effective area (combined with the GPS spreading functions). The GPS ambiguity functions (in both delay and Doppler) increase the effective area of each delay Doppler bin, causing power to be “spread” into adjacent delay and Doppler bins from outside the geometry determined physical scattering area. These functions change the levels of overall processed power observed. The physical area of each DDM bin can be calculated as follows,

$$A_{\hat{\tau}, \hat{f}} = \iint_A dx dy \tag{5}$$

An example of the physical scattering areas per pixel for a typical DDM is shown in Figure 4. Note that points up to and before the specular point bin (i.e. at delays shorter than the specular reflection point delay) have no physical surface scattering area. The power received in the bins before the specular point is due to power being spread into these bins by the GPS ambiguity functions from physical areas near the specular point. The effective surface scattering area for each delay/Doppler bin is expressed as the ambiguity function weighted surface integration,

$$A_{\hat{\tau}, \hat{f}} = \iint_A \Lambda_{\hat{\tau};x,y}^2 S_{\hat{f};x,y}^2 dx dy \tag{6}$$

where the delay spreading function, $\Lambda_{\hat{\tau};x,y}$ and the Doppler spreading function, $S_{\hat{f};x,y}$, are integrated over the physical surface corresponding to each individual delay/Doppler bin. Figure 5 shows the effective scattering area DDM corresponding to the physical scattering areas illustrated in Figure 4.

Initial analysis has shown that when only using a relatively small area of the DDM (corresponding to approximately a 25 km² area on the surface), it is sufficient to approximate the receive antenna gain, range loss terms and the GPS transmit antenna power and gain using constant values calculated at the specular reflection point.

As a standard Level 1 data product, CYGNSS data include DDMs over 11 Doppler bins \hat{f} and 17 delay ($\hat{\tau}$) pixels around the specular point. The NBRCS $\sigma_{\hat{\tau}, \hat{f}}^0$ is calculated as per Equation 4 for each delay/Doppler bin.

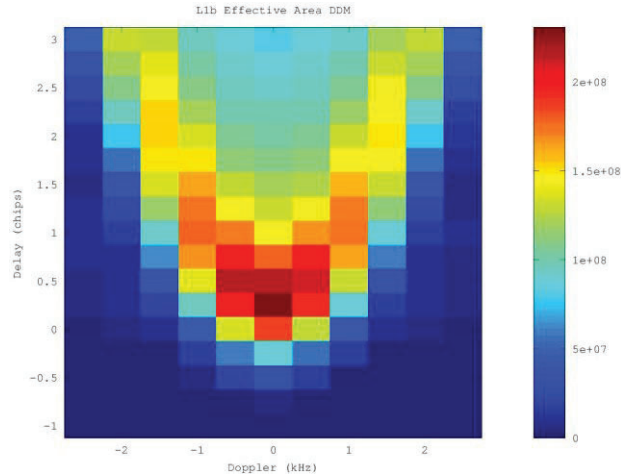


Fig. 5. Effective scattering area corresponding to the physical scattering area shown in Figure 4.

H. Digital to Analog DDM Scaling Issue

In the original CYGNSS L1a calibration algorithm, the entire Level 1a DDM was scaled from digitally sampled DDM values to the equivalent analog sampled power based on the 2-bit analog to digital sample distribution. However, examination of closely geo-located tracks between different observatories at very close time intervals revealed an observed bias between measurements over nearly identical conditions. Figure 6 (left) shows one such case, where FM6 and FM8 pass over nearly the same surface within 5 minutes of each other, yet a clear difference in the NBRCS values can be observed over the length of the track. Upon subsequent investigation, an issue in the analog to digital scaling being applied was found, in which the calculated correction between digital and analog measurements was not correct and introducing significant statistical biases between observatories.

Upon removal of the original digital to analog scaling the overall inter-satellite bias statistics improved significantly. Figure 8 (right) shows the same two tracks after the scaling has been removed, with good agreement across the entire track. A significant reduction in inter-satellite measurement bias was demonstrated with the removal of the digital to analog scaling factor.

I. Calculating a Normalized Bi-static Radar Cross Section

The Level 1b bin by bin DDM of σ and the bin by bin DDM of effective scattering areas can be combined to calculate a normalized radar cross section value, σ_0 , over the DDMA. The CYGNSS Level 2 wind retrieval products use the DDMA to generate geophysical model functions (GMF) to estimate near surface winds. The DDMA consists of 3 delay bins and 5 Doppler bins, with the specular point located in the first row (shortest delay) of this region. Figure 7 shows this DDMA region in red, overlapped with the normal instrument processed DDM delay and Doppler pixels in black. The true (best estimate) of the DDMA region (as calculated by the precise specular point estimation method described above) is marked as a red dot in this figure, while the white dot is the Level 1b DDM that the best estimate specular point falls in.

These precise DDMA bins will not normally align exactly with the L1b DDM bins generated by the instrument (due to errors in the instruments open loop signal tracker) making a simple summation over the 15 central bins in the L1b DDM problematic. The best estimate DDMA radar cross section is the weighted combination of L1b DDM bins around the best estimate surface specular point and fractional contributions from bins outside and adjacent to the DDMA region. This larger set of DDM bins is, when weighted and summed, the best estimate of the multi-bin DDMA total radar scattering cross section σ_0 . The mis-alignment between the instrument generated L1b DDM bins and the best estimate DDMA bins is illustrated in Figure 7. The DDMA specular point is offset by fractional bin amounts in delay (δ) and Doppler (Δ) from the instrument L1b measurement DDM shown in the figure.

In order to calculate the total radar cross section in the red DDMA area, the actual measurement L1b values (one per white box/pixel) need to be combined using a weighting scheme that includes only a fractional amount of power from bins around the edges of the DDMA bins. The fractional weighting scheme used is approximated to be linear in both the delay and Doppler dimensions. Figure 9 shows the regions of overlap for a single red DDMA bin with respect to the surrounding measurement bin values.



The total DDMA radar cross section can be calculated as per Equation 7, resulting in a combined expression for the DDMA σ^0 ,

$$\sigma^0 = \frac{\sigma_{weighted}}{A_{total}} = \frac{W_{i,j} \sum_{i=1}^N \sum_{j=1}^M \sigma_{\tau_i f_j}}{\sum_{i=1}^N \sum_{j=1}^M A_{\tau_i f_j}} \quad (7)$$

where N and M represent the delay and Doppler bin in the L1b DDM, respectively (with N = 4 and M = 6, a single bin more than the DDMA size in both dimensions)

$$\begin{aligned} \sigma_{weighted} = & (1 - \delta)(1 - \Delta)\sigma_1 + (1 - \delta)(\sigma_2 + \sigma_3 + \sigma_4 + \sigma_5) + \\ & (1 - \delta)\Delta\sigma_6 + (1 - \Delta)(\sigma_7 + \sigma_{13}) + \Delta(\sigma_{12} + \sigma_{18}) + \\ & \delta(1 - \Delta)\sigma_{19} + \delta(\sigma_{20} + \sigma_{21} + \sigma_{22} + \sigma_{23}) + \delta\Delta\sigma_{24} + \\ & (\sigma_8 + \sigma_9 + \sigma_{10} + \sigma_{11}) + (\sigma_{14} + \sigma_{15} + \sigma_{16} + \sigma_{17}) \end{aligned} \quad (8)$$

Each bin in the L1b DDM contributing to the weighted $\sigma_{weighted}$ is scaled by a weighting factor $W_{i,j}$ based on the overlap with the respective best estimate DDMA bin. $\sigma_{weighted}$ is then normalized by the sum of the effective area DDMA bins (which consist of the 15 bins centered at the ideal specular reflection point and require no weighting correction) to arrive at the final σ^0 measurement over the DDMA region. The summations and weighting involved in calculating $\sigma_{weighted}$ for the example above is expressed in Equation 8, where the delay and Doppler index values are simplified to single bin numbers as illustrated in Figure 7, and terms with the same weighting factor are combined.

J. Altitude Dependent DDMA Area Normalization

The CYGNSS satellites were launched into slightly elliptical orbits, causing altitude fluctuations between perigee and apogee of up to approximately 35 km. This was not taken into account in the V2.0 calibration algorithm, where a circular orbit at a constant altitude was assumed during the generation of the initial look-up-tables (LUTs) used to perform the scattering area normalization of the DDMA, to arrive at NBRCS estimates of σ^0 . This has been corrected starting in Version 2.1 with an updated normalization area LUT which accounts for the changing altitude of the CYGNSS spacecraft.

After the calculation of the weighted DDMA sigma total as described above, $\sigma_{weighted}$, the bistatic scattering cross section is normalized as shown in Equation 7. In the Version 2.0 version of the calibration this was performed with a look-up-table which was a function of incidence angle and elevation angle only, at a constant altitude. This ignored the effects of the changing satellite altitudes and introduced (relatively) small errors (up to 0.1 dB) into the σ^0 estimation used in subsequent wind speed and MSS retrievals. After Version 2.1, a new LUT was generated with an altitude dimension. This permitted the area normalization to account for changes in the scattering area due to the slight eccentricity of the orbits, as well as longer time scale orbit changes. An example sub-set of the new DDMA normalization areas (reduced to better reveal the changing LUT area magnitudes) is shown in Figure 8 as a function of incidence and altitude (at a constant azimuth angle). Testing of the new altitude dependent LUT has been validated to significantly reduce correlation of σ^0 with the satellite altitude. As of Version 3.2, the LUT altitude range has been extended down to 450 km to account for natural satellite orbit reduction drifting.

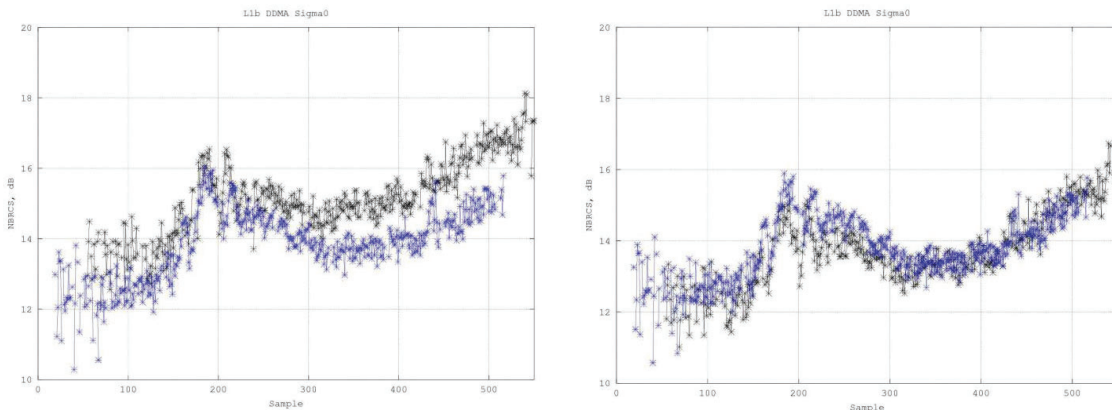


Fig. 6. (left) Inter-satellite bias between tracks of FM6 and FM8 on August 23rd less than 5 minutes apart. (right) After digital to analog scaling removed NBRCS values agree much better across the same ocean track.

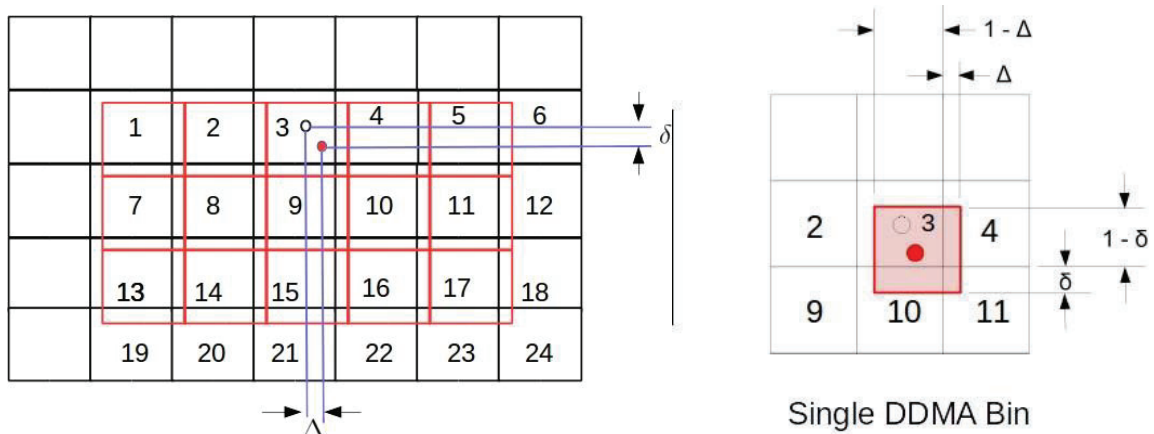


Fig. 7. (left) Level 1b DDM of σ values. Numbered to correspond to same pixels with DDMA overlay and bin numbers referenced to Equation 9. The red group of DDMA bins is the overlay of the 3 by 5 DDMA measurement area with the processed Level 0 DDM pixels, containing a typical mis-alignment. The best estimate DDMA, is based on a refined specular point estimate and represents the true measurement error. (right) Detail of the overlap areas of a single DDMA bin (the specular point bin) and adjacent L1b bins.

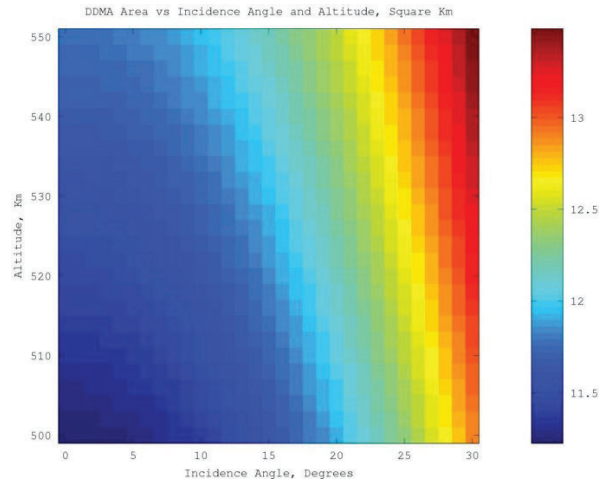


Fig. 8. Version 2.1 DDMA Area LUT values for altitudes between 500 and 550 km (covering the full range of the CYGNSS orbits, with margin on the low side), and incidence angles between 0 and 30 degrees. The increases in DDMA area with incidence angle and altitude are both clearly observable in the new LUTs. These data were generated at a constant 90deg azimuth angle. Color scale is in square kilometers for the entire DDMA region.

K. Characterization of GPS Effective Isotropic Radiated Power (EIRP, v2.1 calibration)

The GPS Transmit Power, P^T and transmit antenna gain, G^T , or the effective isotropic radiated power (EIRP) can be estimated using a combination of ground based measurements and a parametrized model as a function of the transmitter space vehicle (SV) for all GPS satellites. Additional details on the ground based power monitor and dynamic EIRP algorithm estimation can be found in [5, 6].

Transmit Power Estimation: A ground-based GPS constellation power monitor (GCPM) system has been designed, built, calibrated, and operated to measure the direct GPS L1 C/A signal [5]. The calibration subsystem and low noise amplifier (LNA) are implemented on a PID controlled thermal plate with extremely stable temperature control. The measured GPS received power has been found to be highly repeatable, as tested for different satellites of three different block types. The measured EIRPs are verified by DLR/GSOCs independent measurements using a calibrated 30 m dish antenna with 50 dB L-band gain [8].

An optimization algorithm is used to estimate the transmit power of GPS L1 C/A-code by minimizing a cost function based on the difference between an engineering forward model prediction and the measurement of received power. We determine our best estimate of the GPS transmit power for L1 C/A signal by averaging 32 days of estimates of P^T , as given in Table I.



TABLE 1
ESTIMATES OF GPS TRANSMIT POWER (LEVEL 1 C/A) FOR VERSION 2.1

PRN	P^T (dBW)	Block	PRN	P^T (dBW)	Block
1	15.09	IIF	17	16.39	IIR-M
2	13.79	IIR	18	14.04	IIR
3	14.77	IIF	19	13.66	IIR
4	-	-	20	13.48	IIR
5	16.28	IIR-M	21	14.43	IIR
6	15.38	IIF	22	14.39	IIR
7	16.86	IIR-M	23	15.41	IIR
8	15.42	IIF	24	15.03	IIF
9	15.49	IIF	25	15.32	IIF
10	16.28	IIF	26	15.22	IIF
11	13.67	IIR	27	15.34	IIF
12	16.88	IIR-M	28	14.27	IIR
13	13.89	IIR	29	16.84	IIR-M
14	13.2	IIR	30	15.47	IIF
15	16.08	IIR-M	31	16.35	IIR-M
16	13.93	IIR	32	15.87	IIF

It should be noted that:

- 1) The estimated power values are indeed an “effective transmit power”, as the product of the exact transmit power and the transmit system gain correction factor (GCF).
- 2) The accuracy of the estimated power values are dependent on the accuracy of the baseline pattern (5th order power series of transmit antenna gain in [7]) used in the forward model simulation.

Transmit Antenna Gain Estimation: The transmit antenna directivity of IIR and IIR-M block type SVs has been published in [7], while that of IIF block type SVs is unavailable to the public. The baseline antenna pattern used in the Level 1 calibration is a 5th order power series (polynomial fitting) of the azimuthally averaged published antenna pattern for IIR and IIR block and that of the averaged pattern of all 12 SVs using improved antenna panel (4 IIR and 8 IIR-M) for IIF block.

Discussion on GPS Transmitter EIRP Characterization:

- 1) Transmit power and antenna pattern: The high resolution full transmit antenna pattern will be retrieved using the direct GPS signal measured by the CYGNSS zenith antenna, as discussed in [6]. Then the transmit power table will be further updated when the full patterns are applied to the optimization algorithm.
- 2) IIF block type power switching issue: 10 of the 12 IIF SVs switch the power sharing between the components in L1 over US east-coast and back over west-pacific in every orbit. It has been a stable behavior since the first quarter of 2017. In version 2.1, the data measured by IIF block was flagged out. The dynamic EIRP calibration algorithm described here will be applied to subsequent Level 1 calibration versions (starting with version 3.0) and include observations from Block IIF GPS satellites.
- 3) SV retirement for PRN 18: On March 5th, 2018, SVN 54 (operating as PRN 18) retired. SVN 34 (Block IIA) is used for PRN 18 since March 20th, 2018. CYGNSS data using PRN 18 since then is flagged.
- 4) Power redistribution for block IIR-M: A commanded redistribution of transmit power from M-code to C/A-code was performed for the 7 active IIR-M satellites on February 7 and February 8, 2017 [8]. The measured carrier-to-noise



(C/N0) density ratio from different geodetic receivers experienced an approximately 1.5 dB-Hz increase on average. This phenomenon indicates an increase in the L1 C/A-code power for all 7 satellites after the maintenance was performed [9]. This event happened before the CYGNSS satellites were transitioned to science mode. No additional power redistribution for IIR-M satellites is reported since then.

- 5) As GPS Block III satellites are activated, this same EIRP procedure is applied until acceptable calibration LUTs are generated for these new satellites, upon which they are merged into the normal CyGNSS data calibration chain.

L. Zenith EIRP Calibration (Version 3.0 calibration)

The v2.1 L1 calibration algorithm assumed a static value for the GPS transmit power and determined the GPS transmit antenna gain in the direction of the specular reflection point using an off-boresight azimuthal averaged estimate of the individual GPS transmitters. The GPS transmitter off-boresight antenna gains in the v2.1 CYGNSS calibration are based on publicly available pre-launch measured patterns provided by Lockheed-Martin [7]. Additionally, release-controlled pre-launch pattern estimates for the Boeing Block IIF satellites were obtained and used to generate off-boresight gain look up tables for the GPS IIF satellites. For GPS transmitters without pre-launch patterns, an approximate pattern was estimated using the best available information.

Generally, these simplified one-dimensional GPS transmit antenna pattern approximations worked well enough to meet the low wind speed requirements. However, it suffers from a number of known problems which are addressed starting with version 3.0 of the CYGNSS calibration algorithm, including,

- 1) The on-orbit GPS transmitter antenna patterns are known to contain differences from the pre-launch measured patterns, as the pre-launch measurements were not made while attached to the flight spacecraft bus. This most likely resulted in pattern distortions as the antenna interacted with the spacecraft and additional avionics present on the same face as the GPS transmit antenna, which were not considered when the pre-launch measurements were made.
- 2) It is generally understood that multiple GPS transmitters (notable the entire Block IIF satellites) operate using flexible transmit power levels. This occurs when the GPS operations center, without any announcement, will change the transmit power level of a GPS satellite for various but unknown reasons. This results in un-predictable jumps in the transmit power which are not accounted for in the v2.1 calibration algorithm, which assumes a constant transmit power level. These “flex-power” variations on the IIF block satellites necessitated the flagging out of all measurements from IIF satellite, greatly reducing the CYGNSS measurement coverage.

The v3.0 calibration algorithm is designed to greatly mitigate the above two error sources by estimating the GPS transmit power and antenna gain (EIRP) using measurements from the direct (zenith) navigation channel of the CYGNSS delay Doppler mapping instrument (DDMI). By directly monitoring and linking the calibration to the direct observation of the GPS transmitter, the unpredictable flex-power changes can be detected instantly. Additionally, the new calibration technique requires only a ratio of the differences of the GPS EIRP between the direct and reflected instrument channels, resulting in lower uncertainties in the azimuthal asymmetries of the GPS transmit antenna patterns.

The (v3.0) Zenith EIRP Level 1 Calibration algorithm uses the same Level 1 calibration equation to calculate the delay Doppler Map bistatic radar cross section values (repeated below).

$$\bar{\sigma}(\hat{t}, \hat{f}) = \frac{P_g(\hat{t}, \hat{f})(4\pi)^3}{E'_S \lambda^2 G_{SP}^T G_S^R R_S^{Total}} \tag{9}$$

where, the two GPS transmitter terms are combined into a single term expressing the EIRP, E'_S , expanded in Equation 10, consisting of the GPS transmitter power level and the GPS transmitter antenna gain in the direction of the specular point (SP). The combined GPS transmitter EIRP is expressed as,

$$E'_S = P_S^T G_S^T \tag{10}$$

The essential difference in the v3.0 calibration algorithm is that the GPS transmitter EIRP is estimated in real time using observations from the CYGNSS zenith navigation antenna, as opposed to using fixed look up table entries. The Zenith EIRP estimation used in the v3.0 calibration is described below.



Estimating the specular GPS EIRP using Zenith Navigation Signals: Estimating the GPS transmitter EIRP in the direction of the CYGNSS zenith antenna starts with the Friis equation for the received GPS power at the receiver,

$$P_Z = \frac{E_Z \lambda^2 G_Z}{(4\pi)^2 R_Z^2} \tag{11}$$

where, E_Z is the GPS transmitter EIRP toward the zenith CYGNSS antenna, G_Z is the CYGNSS zenith antenna gain, R_Z is the path distance from the GPS transmitter to the CYGNSS satellite. This expression can be rearranged to an expression for the GPS zenith EIRP (E_Z),

$$E_Z = \frac{(4\pi)^2 P_Z}{G_Z \lambda^2 L_Z} \tag{12}$$

Each of the terms in Equation 12 are calculated as,

- 1) G_Z is estimated using the derived CYGNSS zenith antenna gain pattern over the full upper hemisphere of observation angles.
- 2) L_Z is the range loss, calculated from the signal path as $L_Z = 1/R_Z^2$, using the estimated CYGNSS receiver position (from its on-board navigation solution) and the GPS satellite position from the published IGS GPS ephemeris.
- 3) P_Z is the estimated EIRP signal power at the CYGNSS receiver.

The raw power measurement of the zenith signal, $C_Z = I^2 + Q^2$ (in units of counts), is related to the signal power referenced to the input to the DMR by,

$$P_Z = 10^{0.1(a(C_Z,dB)^2 + b(C_Z,dB) + c)} \tag{13}$$

where $C_Z, dB = 10\log_{10}(C_Z)$. The scaling quadratic regression coefficients (a, b, c) are derived from laboratory characterization tests of the EMulator, and P_Z is in units of Watts. The default zenith power conversion coefficients are shown in Table 2 below.

TABLE 2
ZENITH COUNTS TO POWER CONVERSION COEFFICIENTS

Coefficient	Value
a	0.011897122540965
b	-0.509944684931564
c	-1.511603333176575e+02

Subsequently, the EIRP of the GPS transmit signal in the direction of the CYGNSS specular point (ES) can be related to the GPS EIRP in the direction of the zenith antenna (EZ) corrected for the slightly different line of sight between the zenith and specular point directions.

In practice, the GPS EIRP towards the specular point can be calculated as a function of the LNA analog gain ratio and the ratio of the GPS EIRP values due to slightly different viewing geometry. Resulting in the following expression for the GPS EIRP towards the specular point,

$$E_S = E_Z \frac{E_S}{E_Z} = E_Z [SZR_E] \tag{14}$$

where,

- E_S/E_Z is the ratio of the specular channel GPS EIRP and the zenith channel EIRP, and is a function of the GPS transmitting Space Vehicle (SV) and the specular reflection incidence angle (theta).
- The SZR_E is the Specular to Zenith Ratio for E_S/E_Z , which is a function of the GPS transmitter and specular point incidence angle.



The specular-to-zenith EIRP ratio (SZR_E) is the azimuthally integrated ratio of the GPS transmit antenna gain in the direction of the zenith antenna to the gain in the direction of the specular reflection point, expressed as,

$$SZR_E(SV, \theta) = \int_0^{2\pi} \frac{G_Z^T(SV, \theta, \Phi)}{G_S^T(SV, \theta, \Phi)} d\Phi \quad (15)$$

where Φ is the azimuth coordinate of the GPS antenna gain pattern. The SZR ratio is a function of GPS SV number and of the incidence angle (θ) of the specular reflection point.

The SZR_A is determined using the pre-launch characterized LNA gain vs temperature look-up-tables. The SZR_E is estimated with empirically determined GPS transmitter antenna patterns, and converted to a look-up-table as a function of the specular point incidence angle for all GPS transmitters as a function of their SV number. For each measurement, the PRN number is converted to SV number from the latest available mapping of SV to PRN.

Finally, the estimated value of E'_S is substituted into the L1b calibration equation 1 and used to generate the L1b BRCS DDM.

M. Rescaling of Nadir Antenna Patterns

Version 2.1 Nadir Antenna Corrections: Prior to launch, antenna pattern measurements were made for all of the port and starboard antennas. In addition, the predicted effects of the spacecraft body were extensively modeled using pattern simulation tools to attempt to accurately predict the final antenna patterns when attached to the spacecraft. These simulations included mechanical CAD models of the physical spacecraft with electromagnetic field simulations using the FEKO and Savant software packages. Additionally, full pattern measurements of the port and starboard antennas were made while mounted to a CYGNSS Engineering Model (EM) in an anechoic chamber. From the modeling effort, which was confirmed by the EM chamber measurements, we know that the solar panels have a significant impact on the observatory antenna gain patterns. The individual modeled pattern measurements were adjusted using a constant gain factor based on measured differences between the flight antennas to create the at-launch gain patterns for each CYGNSS flight model (FM) antenna calibration tables.

However, we know that there is potentially significant variability in the exact deployed positions of the solar panels from repeated pre-launch panel deployment tests. It therefore stands to reason that applying a simple constant offset for each of the FM antennas from the modeling and EM measurements is overly simplistic. It was evident from the initial analysis of the CYGNSS on-orbit data that an improved estimate of the CYGNSS antenna patterns was needed for each antenna in the constellation.

σ_0 is expected to vary as a function of wind speed and geometry, so σ_0 anomalies are computed as the difference between each calibrated σ_0 from the mean value for all σ_0 within 2 meters per second wind speed and 2 degree incidence angle bins. Reference wind speeds are from collocated ECMWF reanalysis fields [13] to within 90 minutes and 25 kilometers of the corresponding CYGNSS observations. To determine the dependence of these anomalies on azimuth angle, average anomalies were computed in 1 degree azimuth bins.

On-orbit estimates of $\sigma_{0,anom}$ described above have been calculated for all CYGNSS flight antennas. For each flight antenna in the constellation (1 port and 1 starboard antennas for each of 8 spacecraft = 16 total antennas), $\sigma_{0,anom}$ anomalies were computed in 1 degree increments of spacecraft off-nadir and azimuth angle. These antenna correction maps were then smoothed over 5 degree windows in azimuth and off-nadir angle in order to reduce measurement noise. These results were then interpolated using nearest neighbor interpolation to a resolution of 0.1 degree. This map of $\sigma_{0,anom}$ as a function of antenna coordinates was used to scale the original patterns to produce a new estimate of the receive pattern gain, which greatly reduced the observed azimuthal anomalies (anomaly subtracted from original antenna pattern in logarithmic space from estimates of gain in dB). This was done for all 16 operational flight antennas on all 8 observatories for Version 2.1.

The resulting $\sigma_{0,anom}$ anomalies gain maps as a function of azimuth averaged across all 8 spacecraft is shown in Figure 9, with example nadir antenna patterns before and after correction shown in Figure 10. The anomalies, which were initially greater than as 40% are reduced to less than 20% residual anomalies across all azimuth angles. The regions near the azimuth angles where most measurements are taken (90 and 270 degrees for Starboard and Port, respectively) have errors reduced to 10% or less. The remaining errors are most likely due to variability within the data not related to wind speed, incidence angle, or receiver antenna pattern effect accounted for in this analysis.

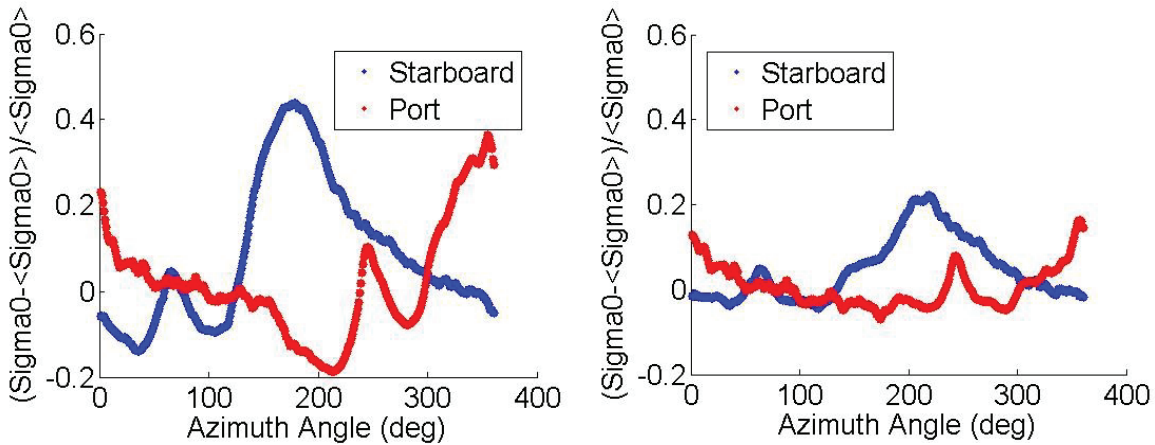


Fig. 9. (left) σ_0 anomalies computed for Level 1 data between day of year 77 and 121 of 2017 on the Version 1 using pre-launch estimated receive antenna patterns. (right) σ_0 anomalies computed for Level 1 Corrected data for Version 2 of the L1 calibration. The anomalies reduce the worst case error of 40% to less than 10%.

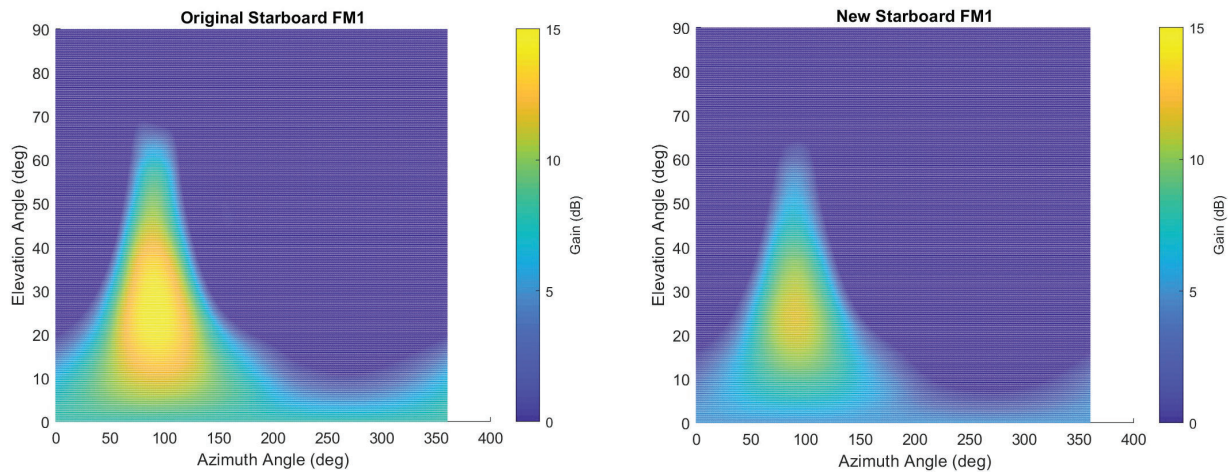


Fig. 10. Original (left) and updated (right) antenna patterns for CYGNSS satellite 1 starboard antenna. Other antenna pattern rescaling are similar. Peak gains were reduced by about 3 dB.

It should also be noted that off-nadir angle is highly correlated to incidence angle for a given spacecraft orientation, with the relationship directly tied to the spacecraft roll, which changes periodically as the spacecraft are adjusted to maintain a power positive orientation for high solar beta angles.

Version 3.0 Nadir Antenna Corrections: As noted above, Version 2.1 of the CYGNSS data includes a rescaling of the at-launch assumed nadir antenna patterns based on matchups of CYGNSS derived L2 winds with model-based matchups. These L2 estimates are based on empirically derived geophysical model functions connecting L1 normalized bi-static radar cross-section (NBRCS) estimates that are themselves based upon the antenna patterns and model-based matchups themselves. In order to place the antenna pattern rescaling on a more physically sound basis, the Version 3 antenna patterns were rescaled using matchups with model-based estimates of MSS.

The relationship between MSS as a function of incidence angle θ is given by:

$$NBRCS(\theta) = \frac{|R|^2}{MSS} \tag{16}$$

Where R is the Fresnel coefficient evaluated at θ . For the version 3 antenna pattern rescaling, matchups between IFREMER WaveWatch III (WW3) estimates [14] of MSS and CYGNSS data were created for all data in 2019 with the CYGNSS data filtered by the overall Level 1 quality control flag.



In order to match the wave spectra of CYGNSS derived MSS, the tail of the IFREMER MSS spectra were extended assuming an Elfouhaily wave spectrum. With this extended WW3 MSS, a model based NBRCS was computed using Equation 16. For each CYGNSS, WW3 MSS matchup, the mean ratio of the observed to model NBRCS was computed in 1 degree bins of antenna elevation and azimuth angle for all 16 CYGNSS nadir antennas (port and starboard antennas of all 8 satellites) within a range modelled NBRCS of 30-40, which contains 20% of the observed data while focusing on the peak of the NBRCS distribution. This ratio has mode of 0.5, leading to a resulting rescaling of the antenna patterns of around 3 dB. The resulting antenna pattern version for v3.1 was v17.

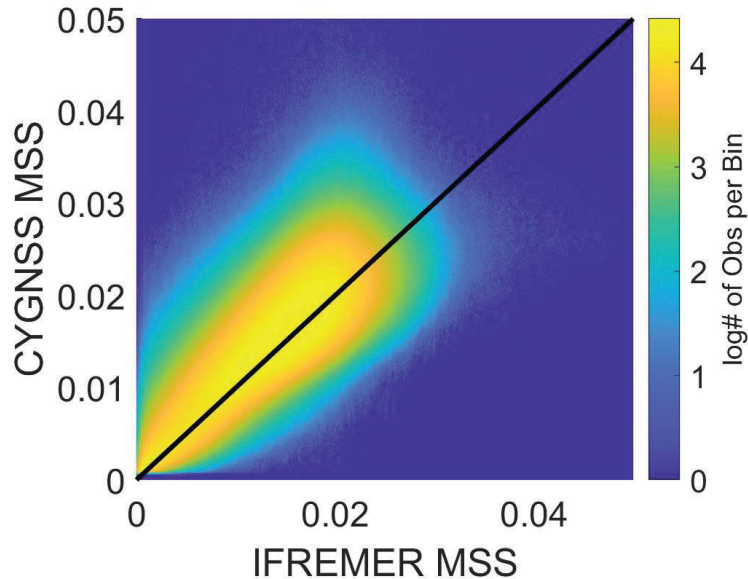


Fig. 11. Comparison of CYGNSS and reference IFREMER MSS

Version 3.2 Nadir Antenna Corrections: Due to the uncertainties in the mapping from model based MSS to GNSS-R wavenumber matched MSS, version 3.2 corrections use an empirical method where each antenna pattern was rescaled in 1 degree azimuth and elevation bins with a 3 degree smoothing window by the ratio of the mean NBRCS from the given pattern to the mean across all 16 antennas. For this, data were limited to only those for which ERA-5 winds were between 5 and 9 m/s when the instruments were nadir pointed and the star tracker was locked. The pre-launch patterns were used as the starting point. The resulting antenna pattern is v20. Figure 12 shows azimuth and elevation cuts for the FM 8 starboard antenna. Results for other antennas are similar.

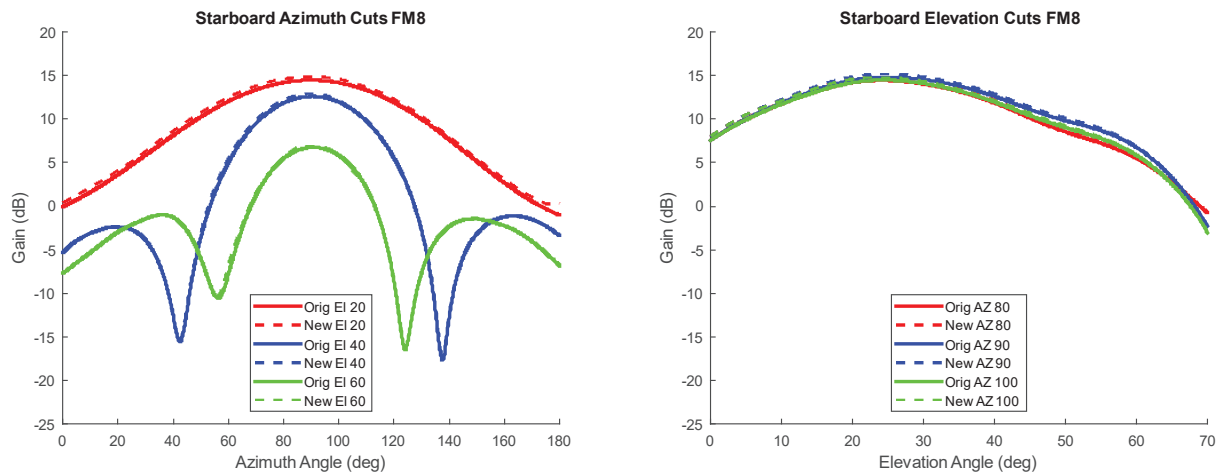


Fig. 12. Azimuth (left) and elevation (right) cuts for the FM 8 starboard antenna (others are similar). The original (solid) and new (dashed) patterns are shown for three different cuts near peak gain (30 degrees elevation, 90 degrees azimuth).



N. NBRCS and EIRP Normalization

In addition to rescaling the nadir antenna patterns, comparisons of the CYGNSS observed NBRCS as a function of transmitter (GPS SV) and receiver (CYGNSS antenna and FM) to the mean NBRCS demonstrated significant variability from SV to SV and FM to FM for not just the NBRCS, but also the SV dependent EIRP going into the calculation of NBRCS. For this reason, normalization of the EIRP and NBRCS is completed prior to their use in computing the observed NBRCS. This additional normalization (or de-biasing) step is applied to L1 calibration versions 3.1 and 3.2, while L1 calibration versions 2.1 and 3.0 included only empirical antenna pattern corrections as detailed in the previous section.

For the NBRCS normalization, a significant dependence of the NBRCS upon incidence angle that varied from receiver to receiver and SV to SV was noted in the data. Due to this, the computed NBRCS are normalized by SV, FM, antenna (starboard, port) and incidence angle in 1 degree increments using data from 2019.

On February 14 of 2020, the flex power mode for the GPS constellation changed significantly, such that the EIRP of the II-RM block satellites shifts noticeably relative to data prior to this date. Because of this, the EIRP for the II-RM SVs is rescaled to match that of the data prior to this change to avoid a discontinuity in CYGNSS NBRCS at that date. This was achieved by normalizing the post Feb 14, 2020 data to the pre-change data by the ratio of the mean of all block II-RM NBRCS data pre- and post-changed.

Version 3.1 and 3.2 NBRCS Normalization: With the new antenna patterns as described above, the NBRCS were rescaled as a function of FM, nadir antenna (starboard/port), SVN, and incidence angle (in 1 degree bins) with respect to the mean NBRCS across all FMs, nadir antennas, and SVN. Incidence angle dependence is tied to the IFREMER model based MSS described above. Figure 13 shows resulting NBRCS histograms as a function of FM and GPS block type for starboard antennas (port similar).

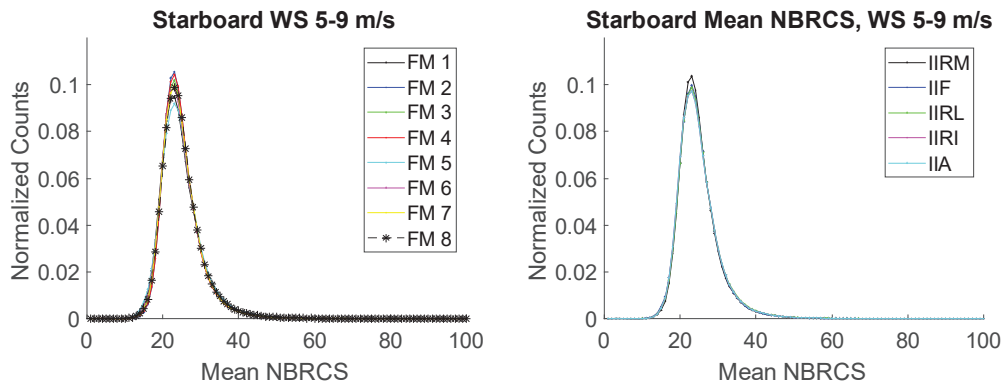


Fig. 13. Mean NBRCS histograms by FM (left) and GPS block type (right) for winds between 5 and 9 m/s for starboard antennas.

II. CYGNSS LEVEL 1 ERROR ESTIMATION METHOD

This analysis assumes that the uncertainties in the CYGNSS Level 1 calibration algorithm are generally independent uncorrelated error sources, which can be characterized with a zero mean Gaussian distribution. This may not be strictly the case for some terms (most notably the GPS transmit power levels), yet to a first order this analysis serves to bound the expected error and as shown in the top-down analysis in Ruf et al [10] is consistent with the best estimate of the overall on-orbit observed CYGNSS wind retrieval performance. The method for this error analysis is based on the partial derivative method presented in Jansen et. al [11]. Additionally, the rolled up error was simulated using a Monte Carlo simulation and was in agreement with the partial derivative estimated error levels presented below.

For more details on the partial derivatives for individual error terms in the L1a calibration equations refer to Gleason et al [12].



A. Error Analysis Methodology

The total error in the L1a or L1b calibrated DDM is the root of sum of squares (RSS) of the individual errors sources in the independent terms of their respective expressions, which can be expressed generically as,

$$\Delta L_1^{a,b} = \left[\sum_{i=1}^x [E(q_i)]^2 \right]^{1/2} \tag{17}$$

where $\Delta L_1^{a,b}$ are the L1a and L1b estimated error values, x is the number of independent errors terms and q_i are the respective input error parameters. The individual errors terms can be estimated by taking the partial derivatives of the calibration equation such that each error term in the process can be quantized as,

$$E(q_i) = \left| \frac{\partial L_1^{a,b}}{\partial q_i} \right| \Delta q_i \tag{18}$$

B. Rolled Up On-Orbit Level 1 Calibration Errors

The wrapped up errors of the Level 1b calibration can be expressed in a similar manner, with the total L1a error rolled in, and estimated over the DDMA region of the DDM (3 delays x 5 Dopplers),

$$\bar{\sigma}_{DDMA}^0 = \frac{P_{g,DDMA} (4\pi)^3 L_{atm}}{P^T \lambda^2 G_{SP}^T G_{SP}^R R_{SP}^{Total} A_{DDMA}} \tag{19}$$

Substituting this equation into Equation 22 results in,

$$E(q_i) = \left| \frac{\partial \bar{\sigma}_{DDMA}^0}{\partial q_i} \right| \Delta q_i \tag{20}$$

where the error terms are: $q_1 = P_g$ (rolled up L1a errors), $q_2 = DDMA_{crop}$, $q_3 = L_{atm}$, $q_4 = R_{SP}^{Total}$, $q_5 = P^T$, $q_6 = G_{SP}^T$, $q_7 = G_{SP}^R$, $q_8 = A_{DDMA}$, respectively.

The On-orbit estimated Level 1 calibration errors 1-sigma estimates are shown below for each input parameter as well as explanations for each term.

TABLE 3
LEVEL 1B INPUT PARAMETER ERROR ESTIMATES

Error Term	Error Magnitude (at a reference sigma0 of 12)	Comment
$E(P_g)$	0.23 dB	Rolled Up L1a Error [12]
$E(DDMA)$	0.10 dB	Error in DDMA Weighting Algorithm
$E(R_{total})$	0.01 dB	Based on total range error estimates of 2000m (very conservative)
$E(EIRP)$	0.32 dB	GPS Transmitter EIRP error
$E(G_R)$	0.43 dB	Estimated Receiver Antenna Gain Error From MC Simulation
$E(A)$	0.05 dB	Effective Scattering Area Error, From E2ES

- 1) $E(P_g)$ is the rolled up L1a error from [5].
- 2) $E(DDMA_{crop})$ is an estimate of the error in the DDMA Weighting algorithm detailed above. The weighting algorithm uses a linear interpolation over non-linear DDM bins and this will introduces some error in the cropping of the final value. The value of 0.1 dB is an approximation based on ideal simulations of the DDMA weighting algorithm.



- 3) $E(R_{total})$ is the total error due to mis-estimation of the path loss from the GPS transmitter to the specular point to the receiver. Given the relatively high accuracies of all three of these parameters, this error is expected to be negligible. More details on the contribution due to the single frequency GPS receiver position estimation performed on CYGNSS can be found in [15].
- 4) $E(EIRP) = E(P^T) + E(G^T)$ is the error in the GPS transmit power and antenna gain correction. The best estimate for this error is based on the top down analysis reported in [6].
- 5) $E(G^R)$ is the error in the receive antenna gain and is based on the analysis of σ_0 anomalies described above, after the described corrections to the receive antenna patterns were applied. The antenna gain error was estimated using Monte Carlo simulations based on the predicted statistical spacecraft attitude performance and best estimate of the receive antenna gain pattern.
- 6) $E(A)$ is the estimated error in the effective scattering normalization area used to convert σ to σ_0 . The CYGNSS End-to-End Simulator was used to generate the look-up-tables used to generate these values. Given the extensive validation of the E2ES this error was at a relatively low value, driven by errors introduced due to the integration step size used in the table generation, plus a small amount of margin.

C. Rolled up L1 Uncertainty

The rolled up L1 uncertainty included in the official data products are a function of multiple terms all of which are impractical to include in a per observation look up table. For this reason the L1 uncertainty included with each L1 σ_0 estimate in the CYGNSS official products is considered only the magnitude of the σ_0 . The total error in the L1 calibration is estimated to be 0.74 dB (1-sigma) and 0.59 dB (1-sigma), at reference σ_0 values of 20 (~14 m/s winds) and 12 (~8.5 m/s winds), respectively. A more detailed breakdown of the error components can be found in [1].

III. CONTINUED L1B ALGORITHM UPGRADES

A. DDMA normalization area re-scaling

Using the CYGNSS End-to-End simulator, estimates of the physical scattering areas and effective scattering areas under varying observation geometries are derived and used to generate a reference A_{tot} LUT for use in the normalization of DDMA radar cross section estimates. An example of this is shown in Figure 14 where surface delay-Doppler solutions are developed on a high resolution (50 meter) grid and subsequently used to identify surface grid pixels corresponding to a given delay τ - Doppler f pair.

It is noted that the determination of the relevant areas is limited to resolutions of ~0.25 chips and ~500 Hz to match the delay $\Delta\tau$ Doppler Δf resolutions of the Level-1 DDM. The original scattering area estimates were based on a forward binning scheme where the physical scattering area at delay τ and Doppler f comprises the footprint spanning $\in [\tau + \Delta\tau, f + \Delta f]$. It follows that the maximum delay/Doppler binning errors associated with the estimation of the physical area (5) are comparable to $\Delta\tau$ and Δf , respectively.

Figure 15 suggests that the forward binning scheme appears to lead to an overestimation of scattering areas which in turn reduces CYGNSS NBRCS estimates relative to reference model NBRCS estimates.

The revised DDMA normalization area estimates used as part of CYGNSS's v3.1 data release are derived using the same procedures used in Section IV.B are used while substituting the forward binning scheme with a central binning scheme such that the physical scattering area at delay τ and Doppler f comprises the footprint spanning $\in [\tau - \frac{\Delta\tau}{2} \leq \tau < \tau + \Delta\tau/2, [f - \Delta f/2 \leq f < f + \Delta f/2]]$ thereby limiting maximum delay-Doppler sampling errors to $\Delta\tau/2$ and delta $\Delta f/2$ respectively. An example of the physical area solutions using the revised binning scheme is shown in Figure 16.

It is estimated that the forward binning scheme was associated with a ~22% average overestimation of DDMA normalization areas such that a reduction of A_{tot} significantly improved the correspondence of CYGNSS's NBRCS estimates to reference NBRCS estimates.

As a result of the switch from forward binning to central binning, the resulting effective area normalization of the DDMA was reduced by 22.36% using a constant scale factor applied to all v3.1 DDMA effective area look-up-table entries.



ATBD Level 1B DDM Calibration

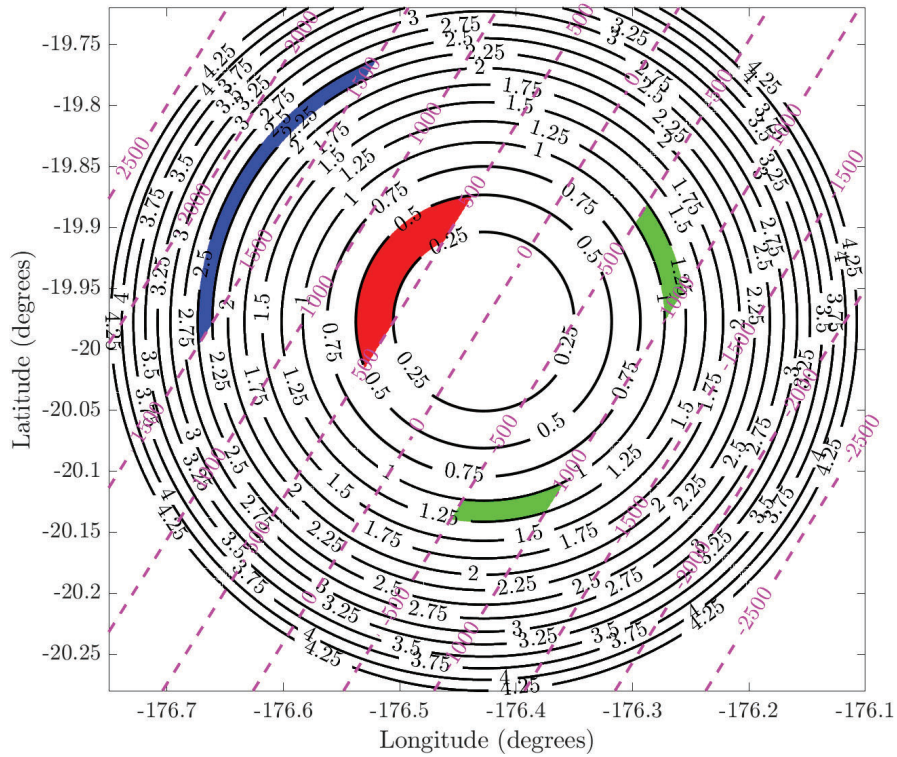


Fig. 14. Example of surface grid used to develop physical scattering area DDMs. Iso-delay (Chips) lines are in black, iso-Doppler (Hz) lines are in magenta. For illustrative purposes, the physical area using a forward binning scheme corresponding to $A(\tau=0.25$ chips, $f = 500$ Hz) is in red, $A(\tau=1$ chips, $f = 1000$ Hz) is in green and $A(\tau=2.25$ chips, $f = 1500$ Hz) is in blue.

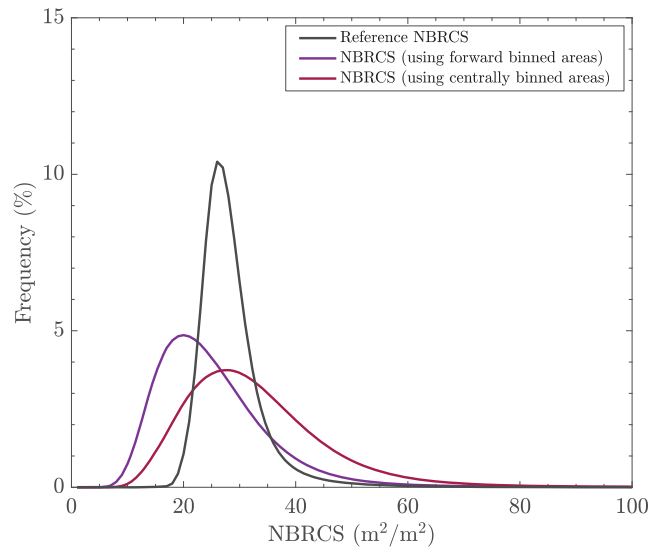


Fig. 15. NBRCS PDFs summarizing the effects of revised DDMA normalization area estimates

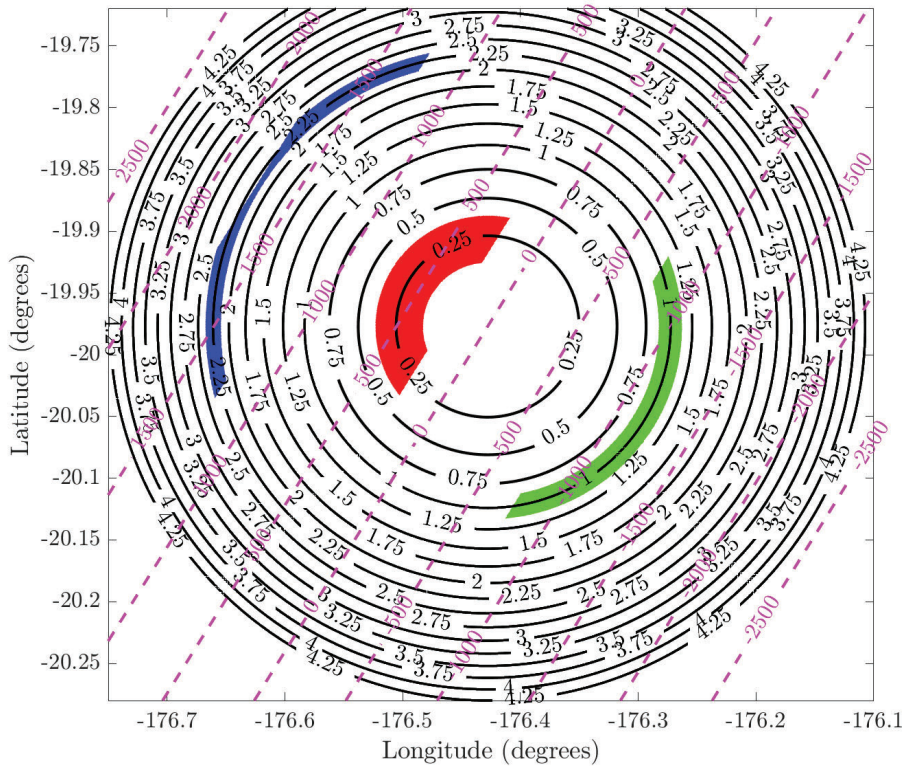


Fig. 16. Example of surface grid used to develop physical scattering area DDMs. Iso-delay (Chips) lines are in black, iso-Doppler (Hz) lines are in magenta. For illustrative purposes, the physical area using a central binning scheme corresponding to $A(\tau=0.25$ chips, $f = 500$ Hz) is in red, $A(\tau=1$ chips, $f = 1000$ Hz) is in green and $A(\tau=2.25$ chips, $f = 1500$ Hz) is in blue.

B. Long Duration Periodic Temperature Correction

A periodic oscillation of CYGNSS’s ocean NBRCS estimates was observed using a multi-year CYGNSS data record. Because a number of known geophysical phenomena, whose sensing is of interest, also oscillate on similar time scales it is crucial to correct for the instrument (L1 calibration) component of this oscillation which in turn is expected to aid in distinguishing clearly between an (internal) thermally generated signal and an (external) geophysical signal. The former requires correction and the latter is a valid science signal and should not be “corrected”. In order to separate these two phenomenon the thermal oscillation correction isolated to the zenith signal only (which does not contain any surface reflected signal).

This strategy relies on the assumed correlation of the thermal oscillation on the zenith signal and that on the nadir science channels. The design and performance of this correction is explained in more detail below.

Characterizing the Observed EIRP/NBRCS Fluctuations: Given complications associated with disentangling ‘true’ surface oscillations with uncompensated thermally driven oscillations, whose correction is of interest, the design and assessment of the related algorithm is explored in the context of zenith channel observables (namely EIRP). The impact of the correction is subsequently evaluated using nadir channel observations, namely NBRCS.

The impact of observed, uncorrected, oscillations on measured EIRP using CYGNSS’s zenith channels is depicted in Figure 17 using a multi-year data record (pre-v3.2).

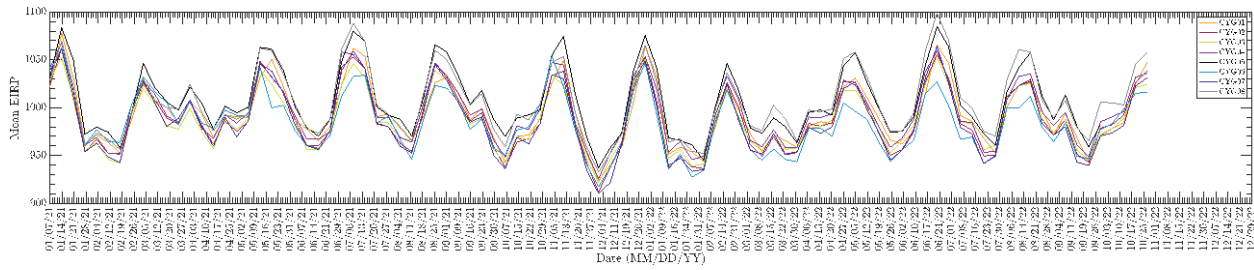


Fig. 17. Time series of oscillations observed in the zenith EIRP measurements for all 8 CyGNSS satellites over the period 2021-2022.

Figure 17 clearly shows periodic EIRP fluctuations of approximately 200 W as a function of time. The potential for the observed oscillations to be an artifact of fortuitous or commanded GPS transmit power variability over similar time scales was ruled out through an analysis of NOAA's Continuously Operating Reference Stations (CORS) reported GPS signal intensities over similar time scales. While it is acknowledged that a 1-1 mapping of measured in situ GPS powers using individual CORS stations and those measured by CYGNSS is inherently limited by a variety of factors, the example depicted in Figure 18 highlights a highly limited power variability over a multi-year data record and provides no indications of 'real' GPS power oscillations with similar harmonics to those reported by CYGNSS's zenith channels.

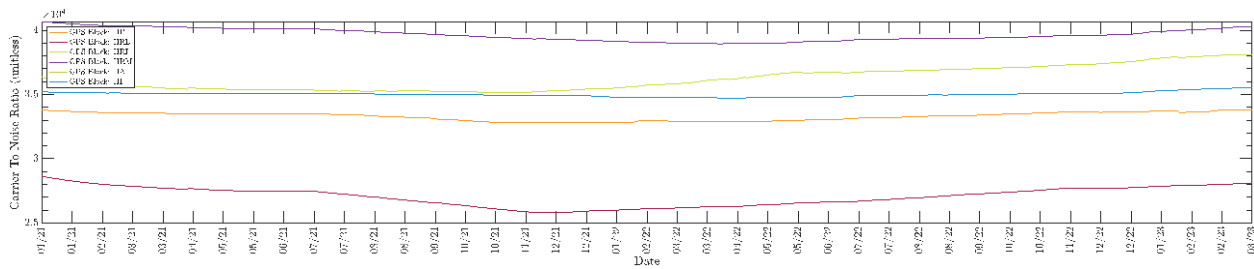


Fig. 18. Time series of CORS station reported GPS carrier to noise ratio over a time period extending from Jan 2021 to March 2023 binned by block-type

It is therefore reasonable to assume that these fluctuations are not inherent in the GPS transmit power which was observed to remain more or less constant over this interval. Additionally, the mean day to day observation geometries of each CyGNSS satellite with respect to the GPS transmitters will remain approximately the same. The effect of slowly changing transmitter geometries, which due to the off-boresight antenna pattern changes could also potentially induce a slow periodic change in the received power at the CyGNSS zenith antenna. This, too, was analyzed and determined to be a second order effect. Therefore, it can be expected that over the period of analysis that the mean daily EIRP observed by each CyGNSS satellite should be very close to constant, with only secondary (noise-like) fluctuations caused by the slowly changing transmitter-receiver geometries. Given the EIRP fluctuations observed over a multi-year data record shown in Figure 16, it can be assumed that an additional (internal) effect is generating the consistently changing received EIRP behavior across all 8 CyGNSS satellites.

How this phenomenon manifests in the NBRCS observations on the nadir science channels is shown in Figure 19.

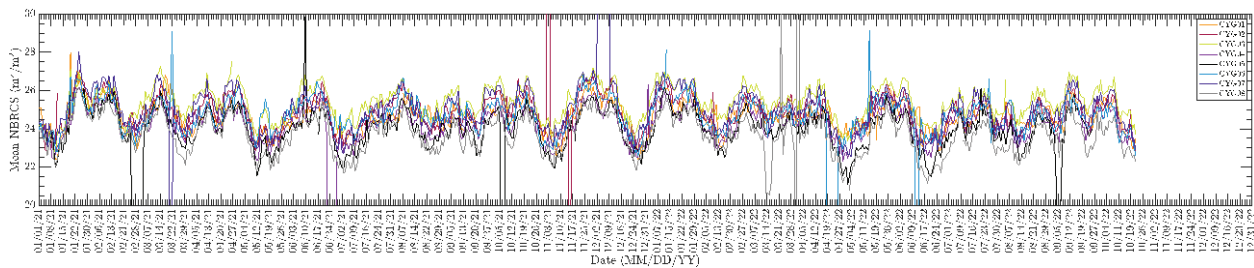


Fig. 19. Time series of oscillations observed in nadir ocean NBRCS measurements for all 8 CyGNSS satellites over the period 2021-2022.

To better characterize the periodicity of the observed oscillation, the frequency spectrum of the NBRCS multi-year time series in Figure 19 is shown in Figure 20.

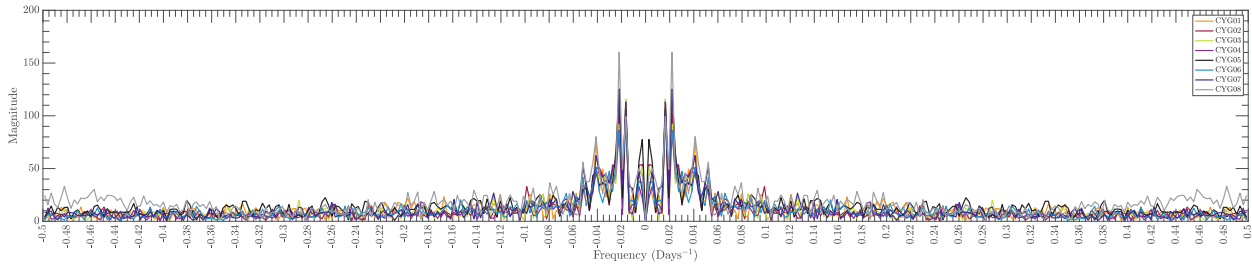


Fig. 20. Frequency Spectrum of NBRCS timeline of Figure 18.

The spectral analysis depicted in Figure 20 clearly shows multiple strong frequency components in the NBRCS time series (at approximately; 25-30 days, 50-60 days, and other intervals), several of which are believed to be (internally) thermally induced while others are likely (external) geophysical phenomenon. By applying a correction to the EIRP only we can be assured of potentially mitigating the adverse impact of the former without degrading the natural signals of the later.

Suspected Root Cause of Thermal Oscillation: The current most plausible theory on the cause of the thermally induced changes in the received power observations on both the zenith and nadir channels is the hypothesis that the antenna S11 parameter is thermally fluctuating. This would represent an additional thermal dependence outside the existing LNA thermal corrections which would not capture these additional fluctuations.

As part of the analysis performed during the development of this correction, we analyzed the effectiveness of using multiple thermal sensors place in different locations on the spacecraft, including both the internal LNA temperature sensor as well as externally sensors on the spacecraft thermal radiators. The radiator sensors are located closer to the antenna/cable interface and proved to be a better reference for the designed corrections, lending credence to the hypothesis that the cause is likely a thermally induced change in a component in the signal chain outside the LNA.

Thermal Oscillation Correction Algorithm: In order to minimize the impact on the L1 calibration processing in the Science Operations Center (SOC) the additional thermal oscillation correction was integrated into the existing Zenith LNA LUT. The correlation of the external radiator temperature and the observed EIRP is shown in Figure 21.

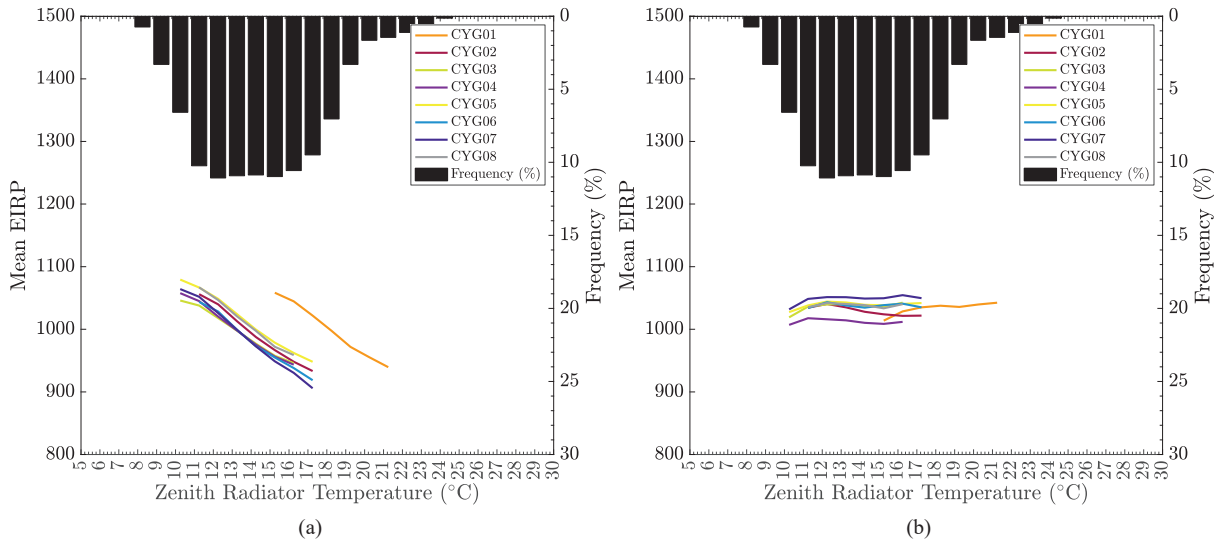


Fig. 21. Mean EIRP vs zenith channel radiator temperature (a) Prior to correction (b) After correction.

The correspondence of uncorrected CYGNSS EIRP estimates (E_Z^i) to radiator temperatures (T_R) is evidenced by the steep slopes in Figure 21(a) across all eight flight modules. To compensate for this effect, a series of zenith channel specific correction factors $f(FM, T_R)$ expressed as a function of (T_R) may be derived that are intended to minimize the slope of E_Z^i vs T_R . The choice to derive an individual correction function for each of the eight receive zenith channels is motivated by their slightly different temperature profiles. The effect of this multiplicative correction is shown in Figure 20(b) where it is observed that the corrected EIRP (E_Z^f) vs T_R slope is reduced by ~90%.



Subsequently, the revised zenith LNA gain (G_{LNA}^f) estimates are updated using:

$$G_{LNA}^f = G_{LNA}^i \cdot \frac{E_Z^i}{E_Z^f} \quad (21)$$

where G_{LNA}^i are the original prelaunch estimates of zenith channel LNA gains vs temperature. The pre and post-correction per-channel gain estimates are depicted in Figure 22.

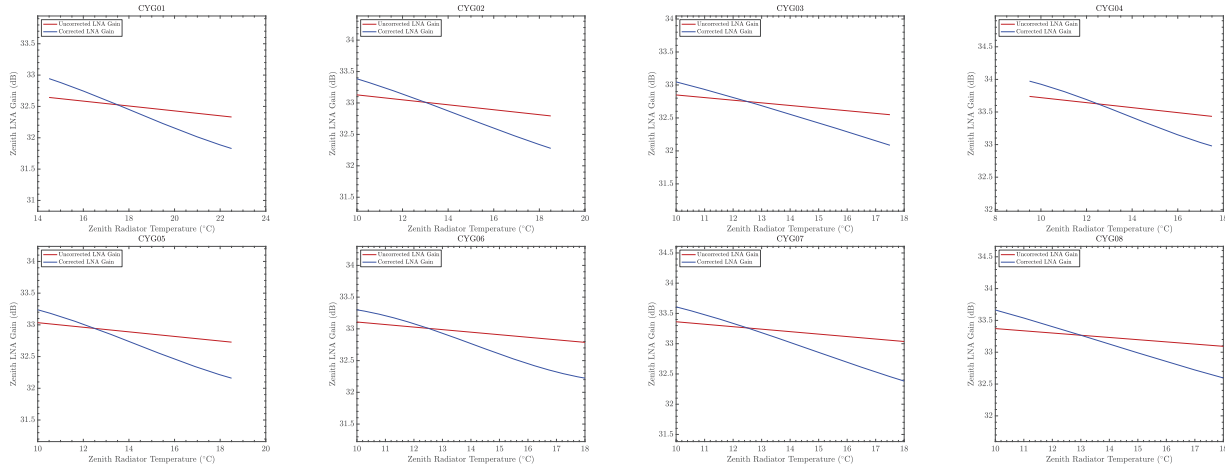


Fig. 22. Per channel zenith LNA gains

Post-Correction NBRCS Behavior: After the application of thermal oscillation correction to the zenith EIRP calculation, the resulting temporal and frequency spectrum behavior of the zenith EIRP and nadir NBRCS observations are shown in Figures 23-24.

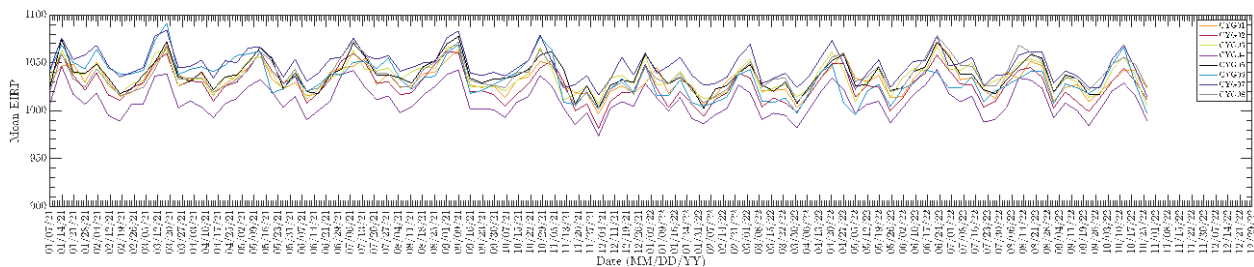


Fig. 23. Time series of oscillations observed in the zenith EIRP measurements after the application of the correction in the form of G_{LNA}^f usage for all 8 CyGNSS satellites over the period 2021-2022.

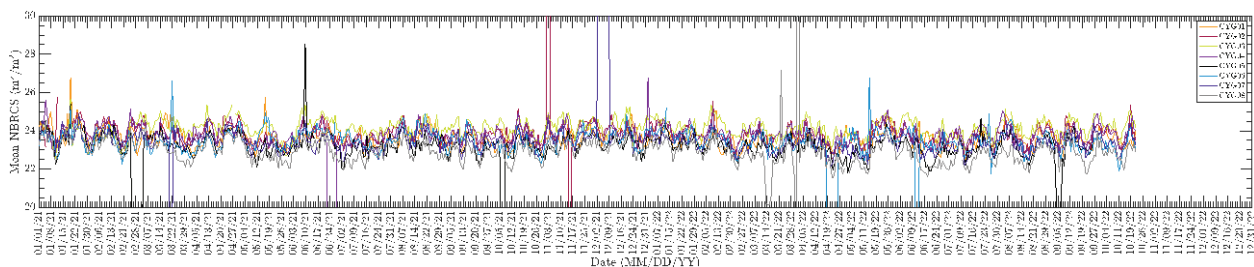


Fig. 24. Updated time series of oscillations observed in nadir ocean NBRCS measurements for all 8 CyGNSS satellites over the period 2021-2022. NBRCS is implicitly corrected through the use of E_Z^f instead of E_Z^i in its calibration.

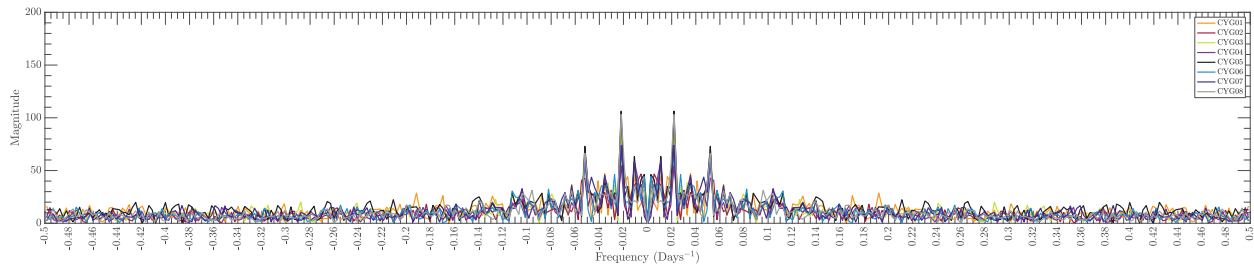


Fig. 25. Updated frequency spectrum of NBRCS timeline of Figure 29. NBRCS is implicitly corrected through the use of E_Z^f instead of E_Z^l in its calibration.

The before and after relative spectral densities corresponding to the 40-60 day window are tabulated in Table 4.

TABLE 4

SUMMARY OF PERIOD OSCILLATION MAGNITUDE BEFORE AND AFTER THERMAL OSCILLATION CORRECTION

CYGNSS Satellite	Before Correction	After Correction	Percent Reduction
FM 1	70.03	54.18	22.63
FM 2	65.89	30.64	53.50
FM 3	64.06	47.10	26.47
FM 4	54.85	44.00	19.78
FM 5	75.76	53.10	29.90
FM 6	68.52	33.54	51.05
FM 7	70.49	38.17	45.85
FM 8	83.42	51.07	38.78

A mean reduction in the peak spectral density of 36% across all 8 CYGNSS satellites of what are believed to have been purely thermal induced L1 instrument error are observed in Table 4. Upon closer inspection of Figures 20 and 25, it can also be clearly observed that several frequency oscillation components have been significantly reduced. It is suspected that the remaining significant frequency spectrum spikes in Figure 25 are likely geophysical effects which we intentionally do not want to “correct”. It is here reiterated that NBRCS is not directly correctly to compensate for these effects. NBRCS is implicitly corrected through the use of E_Z^f instead of E_Z^l in its calibration.

IV. MERGER OF OCEAN AND LAND LEVEL 1 NETCDF PRODUCTS

Beyond CYGNSS’s initial ocean surface emphasis, the swath of disparate land applications its measurements have been used for motivated expanding the scope of Level-1 calibration and validation activities to include the constellation's land observables. Additional calculations have been added specifically for land observations and included in the standard Level 1 released netcdf files. Where applicable, these new calculations have been extended to ocean measurements. The new calculations calculated over all land and ocean observations include an estimate of surface reflectivity (valid in coherent scattering conditions) and a signal coherence estimate which can be used to weight the decision of how users apply the NBRCS and/or Reflectivity estimates based on the signal characteristics and surface conditions. The signal coherency estimator and new land and ocean parameters are described below. For full explanations of the new parameters please see the cited references and the official CYGNSS Data Dictionary.

A. Signal coherency estimator

An algorithm for detecting coherence in CYGNSS DDMs has been developed and is fully described in [25]. Because CYGNSS DDMs report only the observed power without phase information, the algorithm uses estimates of “power ratio” within the pixels of a given DDM to predict coherency. The estimate used is a ratio of the powers in differing portions of the DDM, and is less sensitive to absolute power levels and is applied to CYGNSS Level-0 uncalibrated DDMs.

The basic detector formulation is based on an estimated power ratio between the peak/center pixels and non-peak, non-noise regions of the DDM. The required detection thresholds for the power ratio are determined using matchups with CYGNSS “Raw I/F” mode measurements for which the DDM phase can be computed and used to identify a higher fidelity coherence reference for comparison. Application of the final detector over a large CYGNSS dataset suggests that approximately 8.9% of all inland returns are coherent. Inland regions persistently identified as coherent were found largely to be associated with the presence of water bodies. A smaller set of desert locations apparently having very low surface roughness were also found to be associated with persistent coherence.

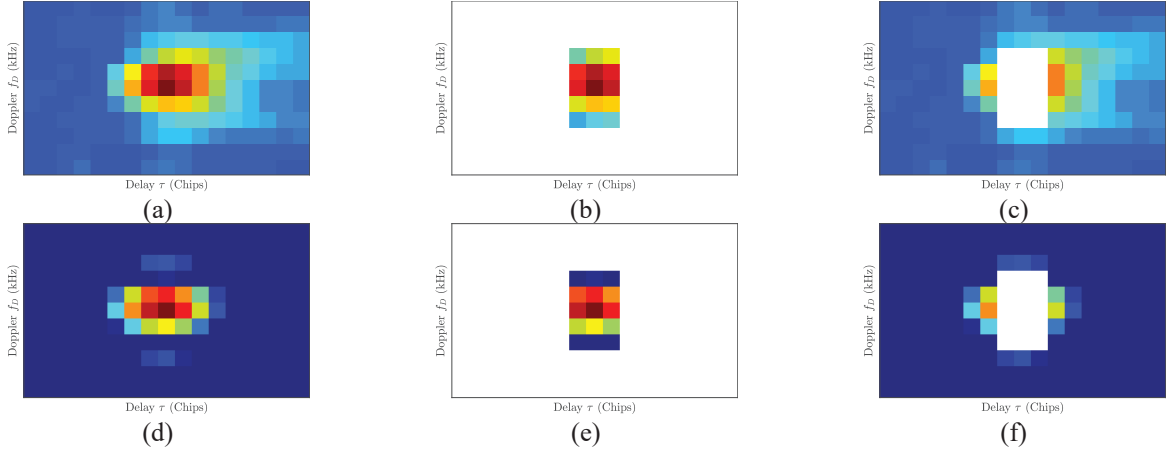


Fig. 26. Illustration of different types of CYGNSS DDMs and detection methodology (a) Incoherent DDM with SNR = 19.05 dB and PR = 0.45 (b) Power within ‘inside’ region of incoherent DDM (c) Power within ‘outside’ region of incoherent DDM (d) Coherent DDM with SNR = 16.07 dB and PR = 3.39 (e) Power within ‘inside’ region of coherent DDM (f) Power within ‘outside’ region of coherent DDM

The detector is also applied to a set of ocean measurements, with the results showing that persistent coherence is limited to areas with sheltered waters. Ocean tests avoiding such regions indicate that the detector’s false alarm rate is approximately 0.0012% for the detection threshold used.

Coherence using CYGNSS’s global Level-1 dataset is detected using the differing “shapes” of DDMs in the coherent and incoherent scattering regimes. In particular, the incoherent scattering associated with rougher surfaces produces power returns to spread over into larger delays relative to that of the specular bin and gives rise to the characteristic “horseshoe” shown in Figure 26(a). In contrast, coherent returns show power concentrated in a sharp peak near the specular bin and a rapid decay in power at bins exceeding ± 0.25 chips in delay and ± 1 kHz in Doppler (Figure 26(d)).

In this method, DDMs are decomposed into two portions. The first includes delay-Doppler pairs within the ± 1 delay bins and ± 2 Doppler bin region about the specular bin, while the second includes all bins outside this region, as shown in Figure 26(b-c) for an incoherent DDM and Figure 26 (e-f) for a coherent DDM. The power ratio (PR) is then computed using:

$$PR = \frac{C_{in}}{C_{out}} \quad (22)$$

with

$$C_{in} = \sum_{i=-1}^1 \sum_{j=-2}^2 DDM(\tau_M + i, f_M + j) \quad (23)$$

$$C_{out} = \sum_{i=1}^{N_\tau} \sum_{j=1}^{N_f} DDM(i, j) - C_{in} \quad (24)$$



Here $N_\tau=17$ is the number of DDM delay bins, $N_f = 11$ is the number of DDM Doppler bins, and τ_M and f_M are the delay Doppler indices of the specular bin respectively. Here τ_M, f_M are selected as those of the DDM bin having maximum power.

Because of the limited power spread in a dominantly coherent scenario the power ratio is expected to be high, while for the incoherent case due to the increased power spread it is expected to be low. To reduce the corrupting impact thermal noise can have on this procedure, a noise exclusion threshold is introduced as a preliminary step prior to computing PR. The noise exclusion thresholds removes varied (noise-only) portions of the Level-1 DDM based on measurement SNR, eliminating pixels expected not to contain information relating dominant scattering regime(s) associated with a given observed surface, while accounting for the increased ‘peakedness’ of both coherent and incoherent DDMs at higher SNRs such that a common coherence detection threshold may be invoked globally. The noise exclusion threshold will also increase the Level-1 coherence metric associated with coherent DDMs whilst leaving that corresponding to incoherent DDMs, relatively, unchanged thereby allowing for a more unambiguous detection process. The detection process ultimately declares DDMs with $PR \geq \rho_o$ as coherent. Note the use of a power ratio in this process reduces the sensitivity to uncertainties associated with calibration of the antenna gains, the GPS transmitted power, and other factors.

Tests over sites conducive to recurrent coherence, high wind ocean observation scenarios known to be conducive to incoherence and comparisons relative to reference Raw I/F coherence detection based methodologies (examples of which are shown in Figure 27) suggested that a detection threshold $\rho_o = 2.0$ was appropriate. The threshold therefore stipulates that the available power within C_{in} (and the 15 delay-Doppler pairs within it) exceeds the power within C_{out} (and the 172 delay-Doppler pairs within it) by at least 100%, thereby requiring a significant concentration of power about the DDM peak to raise the “dominantly coherent” flag for a given DDM. Raw power ratio estimates are also provided to end users as part of CYGNSS v3.2 data release enabling them to invoke a variety of detection thresholds.

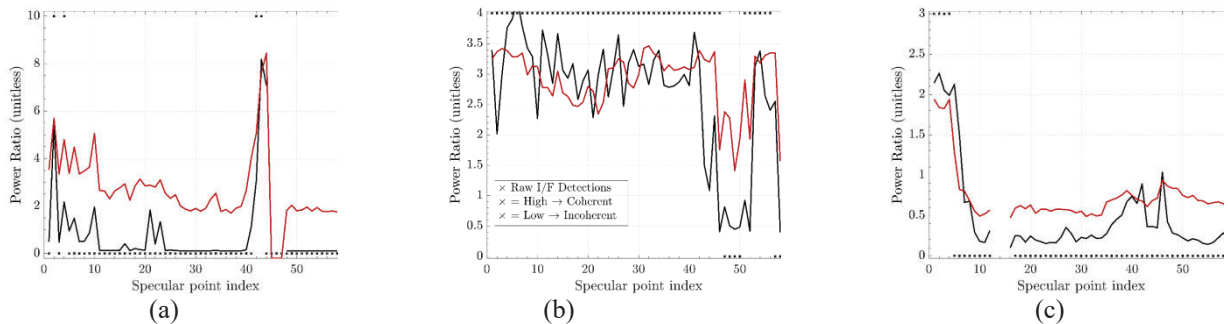


Fig. 27. Comparison of Level-1 DPSD power ratio and matched-filer WAF correlation against Raw I/F coherence/non-coherent detection (a) Track 1, dominantly non-coherent with brief periods of coherence, (b) Track 2, dominantly coherent with brief interval of non-coherence and (c) Track 3, dominantly non-coherent after brief coherent interval at start.



B. Additional land L1 parameters

The following parameters have been added for all CYGNSS land observations based on the existing CYGNSS ocean/land mask.

TABLE 5
ADDITIONAL LAND SPECIFIC LEVEL 1 NETCDF PARAMETERS

Parameter	Description
Reflectivity	Surface reflectivity , calculation described in [17]
Land Geolocation Confidence Flag	Based on three criteria: a) agreement of predicted and detected peak in delay, b) agreement in Doppler, c) Snell reflection angle minimum. See [17] for details and [1] for netcdf state values.
Near Ocean Flags	“Near Ocean” (within 50 km), “Very Near Ocean “ (within 25 km) flags to provide proximity to ocean for land observations.
Coherency Flag	Estimate of signal coherence calculated using method described in [25].
SRTM DEM Altitude and Slope	Surface altitude and relative slope at the estimated land specular point value. Land specular point estimation described in [17].
MODIS Land Cover Type	Land cover type at estimated land specular point. See CYGNSS Data Dictionary [1], for details.
Surface Water Flags	Water flags at the within 1 km, 2 km, 5 km and 10 km of estimated land specular reflection point. Estimated using the Pekel global water mask.
Surface Water Percentage	Percentage of water within 1 km, 2 km, 5 km and 10 km of estimated land specular reflection point. Estimated using the Pekel global water mask.
Local Pekel Water Map	A 5x5 1km resolution local water mask centered at the estimated land specular point. Cropped version of the 1 km averaged localized Pekel water mask.

C. Land Specular Point Calculation

Modification of the specular point calculation over land and quality checks are described in detail in [4]. The overall smoothness and uniformity of the ocean allows for the identification of a single specular reflection point at the minimum path difference between the transmitter, surface and receiver using a WGS84 ellipsoidal representation of the Earth corrected for the mean sea surface height [1]. A similar technique generally works well for flat land surfaces whose heights are not far from the WGS84 approximation and instead of making a fine adjustment based on ocean height variations, a global digital elevation map is used to elevate the estimate specular point from the Earth’s reference ellipsoid.

Using a local surface topography model [26] to adjust the estimated WGS84 specular point to the land surface is adequate for most applications. Generally, for reflections from land with topographic variations, there is occasionally no singular unique specular point as reflections may occur from multiple surface locations separated in delay Doppler space. Given the potential of such conditions, additional criteria are required to assure that the geolocation estimate is sufficiently accurate for science applications. These criteria are;

- 1) Signal Delay Consistency. Quantified based on the predicted and received code phase delay of the actual observation with respect to the expected code phase delay based on the geometry and land specular point estimate.
- 2) Signal Doppler Consistency. The Doppler version of the delay consistency check. Calculated as the difference between expected and received Doppler of the received signal.
- 3) Reflection Geometry Consistency. Calculate based as the difference between the pair of local surface Snell reflection angles.

For a given CYGNSS land DDM, these three conditions are estimated using a local digital elevation map grid centered at the specular reflection point initially estimated using the WGS84 surface model. This initial estimate is then projected to the land surface using a 1 km resolution SRTM digital elevation map [26], as,

$$\vec{S} = \vec{S}_{lat',lon'}^{W84} + \frac{\vec{S}_{lat',lon'}^{W84}}{|\vec{S}_{lat',lon'}^{W84}|} \Delta H \tag{25}$$

where H is the DEM height above the WGS84 ellipsoid at the offset latitude and longitude. The three quality check are subsequently performed on the estimated land specular point estimate.



These checks are computed over a local surface grid around the estimated specular point. If each criteria check is within preset limits for a given grid point, it is likely that this location is correct. Table 5 summarizes the three criteria and the limits applied (more details included in [26]). The limits in Table 5 were selected to achieve an approximate geolocation accuracy of 1 km or less (although results will vary depending on the local terrain variations). The algorithm also assigns a confidence level to each geolocation, as specified in Table 6 based on if the estimated land specular point satisfies all three conditions, as well as an additional criteria on the observed signal to noise ratio. Higher SNR results in more confidence in the first two quality checks by providing a clear indication of the received signal location in delay and Doppler.

TABLE 6
SUMMARY OF LAND GEOLOCATION CONFIDENCE CHECKS

Criteria	Threshold	Verification
Received vs Predicted Delay Difference	2.5 C/A Code Chips (~733m)	Delay Consistency
Received vs Predicted Doppler Difference	200 Hz	Doppler Consistency
Snell Angle Difference	2 Degrees	Reflection Geometry

TABLE 7
SUMMARY OF LAND GEOLOCATION CONFIDENCE CHECKS

SNR Threshold (2 dB)	Quality Checks (All 3)	Confidence Flag	Percentage Land Observations	Comment
Above	Invalid	0	1.3	Most likely incorrect
Below	Invalid	1	21.5	Probably incorrect
Below	Valid	2	28.4	Likely correct
Above	Valid	3	48.8	High probability correct



REFERENCES

- [1] Gleason, S., Ruf, C. Clarizia, M.P., OBrien, A. J., "Calibration and Unwrapping of the Normalized Scattering Cross Section for the Cyclone Global Navigation Satellite System", IEEE Trans. Geoscience and Remote Sensing, Vol. 54, No. 5, May 2016.
- [2] Gleason, S., Ruf, C.S., OBrien, A.J. and D.S. McKague, "The CYGNSS Level 1 Calibration Algorithm and Error Analysis Based on On-Orbit Measurements," IEEE Journal of Selected Topics in Applied Earth Observations and Remote Sensing, 10.1109/JSTARS.2018.2832981, 2018.
- [3] Zavorotny V. and A. Voronovich (2000), Scattering of GPS Signals from the Ocean with Wind Remote Sensing Application . IEEE Trans. Geosci. Remote Sens., Vol. 38, pp. 951-964, March 2000. DOI: 10.1109/36.841977
- [4] DTU Space, National Space Institute (Denmark). Global Mean Sea Surface.
- [5] Wang, T., Ruf, C., Block, B., McKague, D. and S. Gleason, "Design and Performance of a GPS Constellation Power Monitor System for Improved CYGNSS L1B Calibration," IEEE Journal of Selected Topics in Applied Earth Observations and Remote Sensing, accepted for publication.
- [6] T. Wang et al., "Dynamic Calibration of GPS Effective Isotropic Radiated Power for GNSS-Reflectometry Earth Remote Sensing," in IEEE Transactions on Geoscience and Remote Sensing, vol. 60, pp. 1-12, 2022, Art no. 5800512, doi: 10.1109/TGRS.2021.3070238.
- [7] W. A. Marquis, W.A. and D. L. Reigh, "The GPS Block IIR and IIR-M broadcast L-band antenna panel: Its pattern and performance, Navigation, vol. 62, no. 4, pp. 329-347, Dec. 2015.
- [8] Steigenberger, P., Hauschild, A., Thielert, S. and R. Langley, "US Air Force puts more power into GPS Block IIR-M C/A-code, GPS World, vol. 28, no. 4, pp. 8-9, Apr. 2017.
- [9] Thielert, S., Hauschild, A., Steigenberger, P. and R. Langley, "GPS IIR-M L1 transmit power redistribution: Analysis of GNSS receiver and highgain antenna data, Proceedings of the 30th International Technical Meeting of The Satellite Division of the Institute of Navigation, Portland, Oregon, Sept. 2017, pp. 1589-1602.
- [10] Ruf, C.S., Gleason, S. and D.S. McKague, "Assessment of CYGNSS Wind Speed Retrieval Uncertainty," IEEE Journal of Selected Topics in Applied Earth Observations and Remote Sensing, 10.1109/JSTARS.2018.2825948, 2018.
- [11] Jansen, M.A., Ruf, C.S. and S.J. Keihm (1995), TOPEX/Poseidon Microwave Radiometer (TMR): II. Antenna Pattern Correction and Brightness Temperature Algorithm, IEEE Trans. Geosci. Remote Sens., Vol. 33, No. 1, pp. 138-146, January 1995.
- [12] Algorithm Theoretical Basis Document (ATBD): CYGNSS Level 1a DDM Calibration and Error Analysis, October 2023.
- [13] Bechtold, P. Bauer, J.R. Bidlot, C. Cardinali, L. Magnusson, F. Prates and M. Rodwell, "Uncertainty in tropical winds," Meteorology section of ECMWF Newsletter No. 134, Winter 2012/13, pp. 33-37.
- [14] The WAVEWATCH III Development Group (WW3DG), 2016: User manual and system documentation of WAVEWATCH III version 5.16. Tech. Note 329, NOAA/NWS/NCEP/MMAB, College Park, MD, USA, 326 pp.+ Appendices.
- [15] Al-Khaldi, M.M., Johnson, J.T., Gleason, S., Loria, E., O'Brien, A.J. and Y. Yi, "An Algorithm for Detecting Coherence in Cyclone Global Navigation Satellite System Mission Level 1 Delay Doppler Maps", IEEE Transactions on Geoscience and Remote Sensing, Vol. 59, Issue 5, 2021.
- [16] Shuttle Radar Topography Mission (SRTM). Available online: <https://www.usgs.gov/centers/eros/> (accessed on September 25, 2023).
- [17] S. Gleason, A. O'Brien, A. Russel, M. Al-Khaldi, and J.T. Johnson, Geolocation, Calibration and Surface Resolution of CYGNSS GNSS-R Land Observations, Remote Sens. 2020, 12, 8; doi:10.3390/rs12081317.
- [18] CYGNSS v3.2 Level 1 netcdf Data Dictionary. Found directly at https://archive.podaac.earthdata.nasa.gov/podaac-ops-cumulus-docs/cygnss/open/L1/docs/148-0346-10_Level_1_netCDF_Data_Dictionary.xlsx. Also found on the v3.2 product "Documentation" tab at https://podaac.jpl.nasa.gov/dataset/CYGNSS_L1_V3.2



APPENDIX – LEVEL 1 DATA DICTIONARY

netCDF Name	netCDF Long Name	netCDF Type	Units	netCDF Dimensions	Comment
Global Values					
time_coverage_start	<none>	file attribute, string	<none>	<none>	ddm_timestamp_utc of the first sample in the file in ISO-8601 form
time_coverage_end	<none>	file attribute, string	<none>	<none>	ddm_timestamp_utc of the last sample in the file in ISO-8601 form
time_coverage_duration	<none>	file attribute, string	<none>	<none>	The time interval between time_coverage_start and time_coverage_end in ISO1806 form
time_coverage_resolution	<none>	file attribute, string	<none>	<none>	The nominal time interval between samples in ISO1806 form
spacecraft_id	CCSDS spacecraft identifier	short	1	<none>	The CCSDS spacecraft identifier: 0xF7 (247): CYGNSS 1 0xF9 (249): CYGNSS 2 0x2B (43): CYGNSS 3 0x2C (44): CYGNSS 4 0x2F (47): CYGNSS 5 0x36 (54): CYGNSS 6 0x37 (55): CYGNSS 7 0x49 (73): CYGNSS 8 0x00 (0): E2ES 0x0E (14): engineering model 0x0D (15): default 0xFF (255): unknown
spacecraft_num	CYGNSS spacecraft number	byte	1	<none>	The CYGNSS spacecraft number: Ranges from 1 through 8 and 99. 1 through 8 are on-orbit spacecraft. 99 is the CYGNSS end-to-end simulator.
ddm_source	Level 0 data source	byte	<none>	<none>	The source of the Level 0 DDM raw counts and metadata. 0 = End-End Simulator (E2ES) 1 = GPS signal simulator 2 = CYGNSS spacecraft 3 = Source unknown
ddm_time_type_selector	DDM sample time type selector	byte	<none>	<none>	Determines the position of ddm_timestamp_utc relative to the DDM sampling period. Set to "Middle of DDM sampling period" for nominal science operations. Other settings are used for pre-launch testing only. 0 = Start of DDM sampling period (used for pre-launch testing only) 1 = Middle of DDM sampling period 2 = End of DDM sampling period (used for pre-launch testing only) 3 = pvt_timestamp_utc (used for pre-launch testing only)



delay_resolution	DDM delay bin resolution	float	1	<none>	DDM delay bin resolution in chips. One chip is equal to 1/1,023,000 seconds.
dopp_resolution	DDM Doppler bin resolution	float	s-1	<none>	DDM Doppler bin resolution in Hz
l1_algorithm_version	<none>	file attribute, string	<none>	<none>	The version number of the L1 processing algorithm.
l1_data_version	<none>	file attribute, string	<none>	<none>	The version number of the L1 data.
lna_data_version	<none>	file attribute, string	<none>	<none>	The version number of the LNA data lookup table.
eff_scatter_version	<none>	file attribute, string	<none>	<none>	The version number of the effective scattering area lookup table.
nadir_ant_data_version	<none>	file attribute, string	<none>	<none>	The version number of the nadir antenna data lookup table.
zenith_ant_data_version	<none>	file attribute, string	<none>	<none>	The version number of the zenith antenna data lookup table.
ant_temp_version	<none>	file attribute, string	<none>	<none>	The version number of the radiometric antenna temperature lookup table.
prn_sv_maps_version	<none>	file attribute, string	<none>	<none>	The version number of the PRN to SV lookup table.
gps_eirp_param_version	<none>	file attribute, string	<none>	<none>	The version number of the GPS effective isotropic radiated power parameter lookup table
land_mask_version	<none>	file attribute, string	<none>	<none>	The version number of the Earth land mask lookup table.
near_land_mask_version	<none>	file attribute, string	<none>	<none>	The version number of the Earth near-land mask lookup table.
very_near_land_mask_version	<none>	file attribute, string	<none>	<none>	The version number of the Earth very-near-land mask lookup table.
open_ocean_mask_version	<none>	file attribute, string	<none>	<none>	The version number of the open ocean mask lookup table.
ddm_a2d_version	<none>	file attribute, string	<none>	<none>	The version number of the DDM digital to analog power conversion lookup table.
milky_way_version	<none>	file attribute, string	<none>	<none>	The version number of the Milky Way mask lookup table.
fresnel_coeff_version	<none>	file attribute, string	<none>	<none>	The version number of the Fresnel coefficient lookup table.
brcs_uncert_lut_version	<none>	file attribute, string	<none>	<none>	The version number of the BRCS uncertainty lookup table.
ddma_les_sel_luts_version	<none>	file attribute, string	<none>	<none>	The version number of the NBRCS (formerly known as DDMA) and LES bin selection table.
mean_sea_surface_version	<none>	file attribute, string	<none>	<none>	The version of the mean sea surface lookup table.
zenith_specular_ratio_gain_version	<none>	file attribute, string	<none>	<none>	The version of the zenith specular ratio gain lookup table.



zenith_calibration_params_version	<none>	file attribute, string	<none>	<none>	The version of the zenith calibration parameters lookup table.
anomalous_sampling_periods_version	<none>	file attribute, string	<none>	<none>	The version of the anomalous sampling periods lookup table.
noise_floor_correction_version	<none>	file attribute, string	<none>	<none>	The version of the noise floor correction factor lookup table.
zenith_sig_i2_q2_correction_version	<none>	file attribute, string	<none>	<none>	The version of the zenith signal I2 Q2 correction factor lookup table.
ddm_nbrcs_scale_factor_version	<none>	file attribute, string	<none>	<none>	The version of the DDM NBRCS correction factor lookup table.
eirp_scale_factor_version	<none>	file attribute, string	<none>	<none>	The version of the EIRP correction factor for the Feb 14, 2020 power shift lookup table.
bin_ratio_qc_version	<none>	file attribute, string	<none>	<none>	The version of the bin ratio QC correction factor lookup table.
zenith_lna_gain_correction_version	<none>	file attribute, string	<none>	<none>	The version of the zenith LNA gain correction lookup table.
modis_land_cover_version	<none>	file attribute, string	<none>	<none>	The version of the MODIS land cover lookup table.
srtm_dem_version	<none>	file attribute, string	<none>	<none>	The version of the STRM DEM lookup table. Derived from 2018 Global Surface Water Explorer
dtu_10_version	<none>	file attribute, string	<none>	<none>	The version of the DTU10 lookup table.
srtm_slope_version	<none>	file attribute, string	<none>	<none>	The version of the SRTM slope lookup table. Derived from 2018 Global Surface Water Explorer
surface_water_map_version	<none>	file attribute, string	<none>	<none>	The version of the Pekel surface water map lookup table. Derived from 2018 Global Surface Water Explorer
per_bin_ant_version	<none>	file attribute, string	<none>	<none>	The version of the per-bin antenna gain lookup table.
Per-Sample Values					
ddm_timestamp_utc	DDM sample timestamp - UTC	double	seconds since time_coverage_start	sample	DDM sample time. The number of seconds since time_coverage_start with nanosecond resolution. Its position relative to the DDM sampling period is determined by ddm_time_type_selector. Some metadata required for DDM calibration are generated relative to pvt_timestamp_utc or att_timestamp_utc. These metadata are interpolated to ddm_timestamp_utc before being used for DDM calibration. Note that the DDM sampling period is not synchronized with the UTC change of second and can occur at any time relative to the UTC change of second.
ddm_timestamp_gps_week	DDM sample timestamp - GPS week	int	week	sample	The GPS week number of ddm_timestamp_utc
ddm_timestamp_gps_sec	DDM sample timestamp - GPS seconds	double	second	sample	The GPS second of week of ddm_timestamp_utc with nanosecond resolution



pvt_timestamp_utc	PVT timestamp - UTC	double	seconds since time_coverage_start	sample	The spacecraft position and velocity epoch. The number of seconds since time_coverage_start with nanosecond resolution. This is the timestamp of the position and velocity reported by the DDMI. This is also the timestamp of the most recent GPS pulse per second.
pvt_timestamp_gps_week	PVT timestamp - GPS Week	int	week	sample	The GPS week number of pvt_timestamp_utc
pvt_timestamp_gps_sec	PVT timestamp - GPS Seconds	double	second	sample	The GPS second of week of pvt_timestamp_utc with nanosecond resolution.
att_timestamp_utc	Attitude timestamp - UTC	double	seconds since time_coverage_start	sample	The spacecraft attitude epoch. The number of seconds since time_coverage_start with nanosecond resolution. This is the timestamp of the spacecraft attitude reported by the spacecraft attitude determination system.
att_timestamp_gps_week	Attitude timestamp - GPS Week	int	week	sample	The GPS week number of att_timestamp_utc
att_timestamp_gps_sec	Attitude timestamp - GPS Seconds	double	second	sample	The GPS second of week of att_timestamp_utc with nanosecond resolution
sc_pos_x	Spacecraft position X at DDM sample time	int	meter	sample	The X component of the spacecraft WGS84 reference frame ECEF position, in meters, at ddm_timestamp_utc. Fill value is -99999999.
sc_pos_y	Spacecraft position Y at DDM sample time	int	meter	sample	The Y component of the spacecraft WGS84 reference frame ECEF position, in meters, at ddm_timestamp_utc. Fill value is -99999999.
sc_pos_z	Spacecraft position Z at DDM sample time	int	meter	sample	The Z component of the spacecraft WGS84 reference frame ECEF position, in meters, at ddm_timestamp_utc. Fill value is -99999999.
sc_vel_x	Spacecraft velocity X at DDM sample time	int	meter s-1	sample	The X component of the spacecraft WGS84 reference frame ECEF velocity, in m/s, at ddm_timestamp_utc
sc_vel_y	Spacecraft velocity Y at DDM sample time	int	meter s-1	sample	The Y component of the spacecraft WGS84 reference frame ECEF velocity, in m/s, at ddm_timestamp_utc
sc_vel_z	Spacecraft velocity Z at DDM sample time	int	meter s-1	sample	The Z component of the spacecraft WGS84 reference frame ECEF velocity , in m/s, at ddm_timestamp_utc.
sc_pos_x_pvt	Spacecraft position X at PVT time	int	meter	sample	The X component of the spacecraft WGS84 reference frame ECEF position, in meters, at pvt_timestamp_utc. Fill value is -99999999.
sc_pos_y_pvt	Spacecraft position Y at PVT time	int	meter	sample	The Y component of the spacecraft WGS84 reference frame ECEF position, in meters, at pvt_timestamp_utc. Fill value is -99999999.



ATBD Level 1B DDM Calibration

sc_pos_z_pvt	Spacecraft position Z at PVT time	int	meter	sample	The Z component of the spacecraft WGS84 reference frame ECEF position, in meters, at pvt_timestamp_utc. Fill value is -99999999.
sc_vel_x_pvt	Spacecraft velocity X at PVT time	int	meter s-1	sample	The X component of the spacecraft WGS84 reference frame ECEF velocity, in m/s, at pvt_timestamp_utc
sc_vel_y_pvt	Spacecraft velocity Y at PVT time	int	meter s-1	sample	The Y component of the spacecraft WGS84 reference frame ECEF velocity, in m/s, at pvt_timestamp_utc
sc_vel_z_pvt	Spacecraft velocity Z at PVT time	int	meter s-1	sample	The Z component of the spacecraft WGS84 reference frame ECEF velocity, in m/s, at pvt_timestamp_utc
nst_att_status	NST attitude status	byte	<none>	sample	The nano star tracker attitude status. 0 = OK 1 = NOT_USED2 2 = BAD 3 = TOO_FEW_STARS 4 = QUEST_FAILED 5 = RESIDUALS_TOO_HIGH 6 = TOO_CLOSE_TO_EDGE 7 = PIX_AMP_TOO_LOW 8 = PIX_AMP_TOO_HIGH 9 = BACKGND_TOO_HIGH 10 = TRACK_FAILURE 11 = PIX_SUM_TOO_LOW 12 = UNUSED 13 = TOO_DIM_FOR_STARID 14 = TOO_MANY_GROUPS 15 = TOO_FEW_GROUPS 16 = CHANNEL_DISABLED 17 = TRACK_BLK_OVERLAP 18 = OK_FOR_STARID 19 = TOO_CLOSE_TO_OTHER 20 = TOO_MANY_PIXELS 21 = TOO_MANY_COLUMNS 22 = TOO_MANY_ROWS
sc_roll	Spacecraft attitude roll angle at DDM sample time	float	radian	sample	Spacecraft roll angle relative to the orbit frame, in radians at ddm_timestamp_utc
sc_pitch	Spacecraft attitude pitch angle at DDM sample time	float	radian	sample	Spacecraft pitch angle relative to the orbit frame, in radians at ddm_timestamp_utc
sc_yaw	Spacecraft attitude yaw angle at DDM sample time	float	radian	sample	Spacecraft yaw angle relative to the orbit frame, in radians at ddm_timestamp_utc



sc_roll_att	Spacecraft attitude roll angle at attitude time	float	radian	sample	Spacecraft roll angle relative to the orbit frame, in radians at att_timestamp_utc
sc_pitch_att	Spacecraft attitude pitch angle at attitude time	float	radian	sample	Spacecraft pitch angle relative to the orbit frame, in radians at att_timestamp_utc
sc_yaw_att	Spacecraft attitude yaw angle at attitude time	float	radian	sample	Spacecraft yaw angle relative to the orbit frame, in radians at att_timestamp_utc
sc_lat	Sub-satellite point latitude	float	degrees_north	sample	Subsatellite point latitude, in degrees North, at ddm_timestamp_utc
sc_lon	Sub-satellite point longitude	float	degrees_east	sample	Subsatellite point longitude, in degrees East, at ddm_timestamp_utc
sc_alt	Spacecraft altitude	int	meter	sample	Spacecraft altitude above WGS-84 ellipsoid, in meters, at ddm_timestamp_utc
commanded_sc_roll	Commanded spacecraft attitude roll angle	float	radians	sample	Commanded spacecraft attitude roll angle, in radians at ddm_timestamp_utc. This value is updated every 10 seconds from the ENG_HI packet.
rx_clk_bias	GPS receiver clock bias	float	meter	sample	The receiver clock bias (in seconds) multiplied by the speed of light as reported by the DDMI, interpolated to ddm_timestamp_utc, in meters.
rx_clk_bias_rate	GPS receiver clock bias rate	float	meter s ⁻¹	sample	The receiver clock bias rate (in seconds/second) multiplied by the speed of light as reported by the DDMI, interpolated to ddm_timestamp_utc, in m/s.
rx_clk_bias_pvt	GPS receiver clock bias at PVT time	float	meter	sample	The receiver clock bias (in seconds) multiplied by the speed of light as reported by the DDMI at pvt_timestamp_utc, in meters.
rx_clk_bias_rate_pvt	GPS receiver clock bias rate at PVT time	float	meter s ⁻¹	sample	The receiver clock bias rate (in seconds/second) multiplied by the speed of light as reported by the DDMI, at pvt_timestamp_utc, in m/s.
lna_temp_nadir_starboard	Starboard antenna LNA temperature	float	degree_Celsius	sample	The temperature of the starboard antenna LNA at ddm_timestamp_utc, in degrees C.
lna_temp_nadir_port	Port antenna LNA temperature	float	degree_Celsius	sample	The temperature of the port antenna LNA at ddm_timestamp_utc, in degrees C.
lna_temp_zenith	Zenith antenna LNA temperature	float	degree_Celsius	sample	The temperature of the zenith antenna LNA at ddm_timestamp_utc, in degrees C.
ddm_end_time_of_fset	DDM end time offset	int	1e-9 s	sample	For diagnostic use only. See UM document 148-0372 CYGNSS L1 netCDF Diagnostic Variables for more information.
bit_ratio_lo_hi_starboard	Starboard low/high bit counter ratio	float	1	sample	Bin ratio of the of the starboard antenna defined as (plus_1_cnts + minus_1_cnts) / (plus_3_cnts + minus_3_cnts).



bit_ratio_lo_hi_port	Port low/high bit counter ratio	float	1	sample	Bin ratio of the of the port antenna defined as $(plus_1_cnts + minus_1_cnts) / (plus_3_cnts + minus_3_cnts)$.
bit_ratio_lo_hi_zenith	Zenith low/high bit counter ratio	float	1	sample	Bin ratio of the of the zenith antenna defined as $(plus_1_cnts + minus_1_cnts) / (plus_3_cnts + minus_3_cnts)$.
bit_null_offset_starboard	Starboard bit count null offset	float	1	sample	For diagnostic use only. See UM document 148-0372 CYGNSS L1 netCDF Diagnostic Variables for more information.
bit_null_offset_port	Port bit count null offset	float	1	sample	For diagnostic use only. See UM document 148-0372 CYGNSS L1 netCDF Diagnostic Variables for more information.
bit_null_offset_zenith	Zenith bit count null offset	float	1	sample	For diagnostic use only. See UM document 148-0372 CYGNSS L1 netCDF Diagnostic Variables for more information.
status_flags_one_hz	1 Hz status flags	int	<none>	sample	One Hz status flags. These flags apply to all four DDMs. 1 indicates presence of condition. Flag masks: 1 = Milky way in zenith antenna field of view 2 = Sun in zenith antenna field of view 4 = Sub-satellite point over open ocean 8 = Subsatellite point latitude ascending, i.e. sc lat is increasing.
Per-DDM Values					
prn_code	GPS PRN code	byte	1	sample, ddm	The PRN code of the GPS signal associated with the DDM. Ranges from 0 to 32. 0 = reflectometry channel idle. 1 through 32 = GPS PRN codes.
sv_num	GPS space vehicle number	int	1	sample, ddm	The GPS unique space vehicle number that transmitted prn_code.
track_id	DDM track ID	int	1	sample, ddm	A track is a temporally contiguous series of DDMs that have the same prn_code. Each track in the file is assigned a unique track_id starting with one. track_id ranges from 1 to N, where N is the total number of tracks in the file.
ddm_ant	DDM antenna	byte	<none>	sample, ddm	The antenna that received the reflected GPS signal associated with the DDM. 0 = none 1 = zenith (never used) 2 = nadir_starboard 3 = nadir_port
zenith_code_phase	Zenith signal code phase	float	1	sample, ddm	The DDMI-measured code phase of the direct GPS signal for prn_code interpolated to ddm_timestamp_utc. $0 \leq \text{zenith_code_phase} < 1023.0$.
sp_ddmi_delay_correction	Correction to DDMI specular point delay	float	1	sample, ddm	For diagnostic use only. See UM document 148-0372 CYGNSS L1 netCDF Diagnostic Variables for more information.



sp_ddmi_dopp_correction	Correction to DDMI specular point Doppler	float	s-1	sample, ddm	For diagnostic use only. See UM document 148-0372 CYGNSS L1 netCDF Diagnostic Variables for more information.
add_range_to_sp	Additional range to specular point at DDM sample time	float	1	sample, ddm	For diagnostic use only. See UM document 148-0372 CYGNSS L1 netCDF Diagnostic Variables for more information.
add_range_to_sp_pvt	Additional range to specular point at PVT time	float	1	sample, ddm	For diagnostic use only. See UM document 148-0372 CYGNSS L1 netCDF Diagnostic Variables for more information.
sp_ddmi_dopp	DDMI Doppler at specular point	float	s-1	sample, ddm	For diagnostic use only. See UM document 148-0372 CYGNSS L1 netCDF Diagnostic Variables for more information.
sp_fsw_delay	Flight software specular point delay	float	1	sample, ddm	For diagnostic use only. See UM document 148-0372 CYGNSS L1 netCDF Diagnostic Variables for more information.
sp_delay_error	Flight software specular point delay error	float	1	sample, ddm	For diagnostic use only. See UM document 148-0372 CYGNSS L1 netCDF Diagnostic Variables for more information.
sp_dopp_error	Flight software specular point Doppler error	float	s-1	sample, ddm	For diagnostic use only. See UM document 148-0372 CYGNSS L1 netCDF Diagnostic Variables for more information.
fsw_comp_delay_shift	Flight software DDM compression delay shift	float	1	sample, ddm	For diagnostic use only. See UM document 148-0372 CYGNSS L1 netCDF Diagnostic Variables for more information.
fsw_comp_dopp_shift	Flight software DDM compression Doppler shift	float	s-1	sample, ddm	For diagnostic use only. See UM document 148-0372 CYGNSS L1 netCDF Diagnostic Variables for more information.
prn_fig_of_merit	PRN selection Figure of Merit	byte	1	sample, ddm	The RCG Figure of Merit (FOM) for the DDM. Ranges from 0 through 15. The DDMI selects the four strongest specular points (SP) for DDM production. It ranks the strength of SPs using an antenna RCG map. The map converts the position of the SP in antenna azimuth and declination angles to an RCG FOM. 0 represents the least FOM value. 15 represents the greatest FOM value.
tx_clk_bias	GPS transmitter clock bias	float	meter	sample, ddm	The GPS spacecraft (sv_num) clock time minus GPS constellation time in seconds times the speed of light, in meters.
sp_lat	Specular point latitude	float	degrees_n orth	sample, ddm	Specular point latitude, in degrees North, at ddm timestamp utc
sp_lon	Specular point longitude	float	degrees_e ast	sample, ddm	Specular point longitude, in degrees East, at ddm timestamp utc



sp_alt	Specular point altitude	float	meter	sample, ddm	Altitude of the specular point relative to the WGS 84 datum in meters, at ddm_timestamp_utc, as calculated on the ground. Note that an approximated DTU10 mean sea surface height model is used to calculate the specular point altitude.
sp_pos_x	Specular point position X	int	meter	sample, ddm	The X component of the specular point position in the ECEF coordinate system, in meters, at ddm_timestamp_utc, as calculated on the ground. Fill value is -99999999.
sp_pos_y	Specular point position Y	int	meter	sample, ddm	The Y component of the specular point position in the ECEF coordinate system, in meters, at ddm_timestamp_utc, as calculated on the ground. Fill value is -99999999.
sp_pos_z	Specular point position Z	int	meter	sample, ddm	The Z component of the specular point position in the ECEF coordinate system, in meters, at ddm_timestamp_utc, as calculated on the ground. Fill value is -99999999.
sp_vel_x	Specular point velocity X	int	meter s-1	sample, ddm	The X component of the specular point velocity in the ECEF coordinate system, in m/s, at ddm_timestamp_utc, as calculated on the ground.
sp_vel_y	Specular point velocity Y	int	meter s-1	sample, ddm	The Y component of the specular point velocity in the ECEF coordinate system, in m/s, at ddm_timestamp_utc, as calculated on the ground.
sp_vel_z	Specular point velocity Z	int	meter s-1	sample, ddm	The Z component of the specular point velocity in the ECEF coordinate system, in m/s, at ddm_timestamp_utc, as calculated on the ground.
sp_inc_angle	Specular point incidence angle	float	degree	sample, ddm	The specular point incidence angle, in degrees, at ddm_timestamp_utc. This is the angle between the line normal to the Earth's surface at the specular point and the line extending from the specular point to the spacecraft. See UM Doc. 148-0336, CYGNSS Science Data Processing Coordinate Systems Definitions.
sp_theta_orbit	Specular point orbit frame theta angle	float	degree	sample, ddm	The angle between the orbit frame +Z axis and the line extending from the spacecraft to the specular point, in degrees, at ddm_timestamp_utc. See UM Doc. 148-0336, CYGNSS Science Data Processing Coordinate Systems Definitions.
sp_az_orbit	Specular point orbit frame azimuth angle	float	degree	sample, ddm	Let line A be the line that extends from the spacecraft to the specular point at ddm_timestamp_utc. Let line B be the projection of line A onto the orbit frame XY plane. sp_az_orbit is the angle between the orbit frame +X axis (the velocity vector) and line B, in degrees, at ddm_timestamp_utc. See UM Doc.



					148-0336, CYGNSS Science Data Processing Coordinate Systems Definitions.
sp_theta_body	Specular point body frame theta angle	float	degree	sample, ddm	The angle between the spacecraft body frame +Z axis and the line extending from the spacecraft to the specular point, in degrees, at ddm_timestamp_utc. See UM Doc. 148-0336, CYGNSS Science Data Processing Coordinate Systems Definitions.
sp_az_body	Specular point body frame azimuth angle	float	degree	sample, ddm	Let line A be the line that extends from the spacecraft to the specular point, at ddm_timestamp_utc. Let line B be the projection of line A onto the spacecraft body frame XY plane. sp_az_body is the angle between the spacecraft body frame +X axis and line B, in degrees, at ddm_timestamp_utc. See UM Doc. 148-0336, CYGNSS Science Data Processing Coordinate Systems Definitions.
sp_rx_gain	Specular point Rx antenna gain	float	dBi	sample, ddm	The receive antenna gain in the direction of the specular point, in dBi, at ddm_timestamp_utc.
gps_eirp	GPS effective isotropic radiated power	float	watt	sample, ddm	The effective isotropic radiated power (EIRP) of the L1 C/A code signal within ± 1 MHz of the L1 carrier radiated by space vehicle, sv_num, in the direction of the specular point, in Watts, at ddm_timestamp_utc. Variations in GPS transmit power are tracked by the direct signal power measured by the navigation receiver. One second samples are smoothed by a +/- 10 second running average.
static_gps_eirp	Static GPS effective isotropic radiated power	float	watt	sample, ddm	Heritage version of gps_eirp (v2.1 and earlier) that assumed a static value for the power level of the L1 signal transmitted by the GPS satellite, prior to implementation of dynamic gps_eirp monitoring in August 2018.
gps_tx_power_db_w	GPS SV transmit power	float	dbW	sample, ddm	Power input to SV Tx antenna. Referenced from the heritage version of gps_eirp (v2.1 and earlier).
gps_ant_gain_db_i	GPS SV transmit antenna gain	float	dBi	sample, ddm	SV antenna gain in the direction of the specular point. Referenced from the heritage version of gps_eirp (v2.1 and earlier).
gps_off_boresight_angle_deg	GPS off boresight angle	float	degree	sample, ddm	SV antenna off boresight angle in the direction of the specular point



ddm_snr	DDM signal to noise ratio	float	dB	sample, ddm	10log(Smax/Navg), where Smax is the maximum value (in raw counts) in a single DDM bin and Navg is the the average per-bin raw noise counts. ddm_snr is in dB, at ddm_timestamp_utc.
ddm_noise_floor	DDM noise floor	float	1	sample, ddm	For non-black-body DDMs: Is equal to the average bin raw counts in the first 45 delay rows of the uncompressed 20 x 128 DDM, in counts, at ddm_timestamp_utc. For black body DDMs: Is equal to the average bin raw counts in all 128 delay rows of the uncompressed 20 x 128 DDM, in counts, at ddm_timestamp_utc.
ddm_noise_floor_corrected	DDM noise floor corrected	float	1	sample, ddm	The ddm_noise_floor after a correction factor, based on the nadir antenna bin ratio, has been applied.
noise_correction	DDM noise floor correction factor	float	1	sample, ddm	The correction factor applied with ddm_noise_floor = (ddm_noise_floor_uncorrected*noise_correction).
inst_gain	Instrument gain	float	1	sample, ddm	The black body noise counts divided by the sum of the black body power and the instrument noise power, in count/W, at ddm_timestamp_utc.
lna_noise_figure	LNA noise figure	float	dB	sample, ddm	The LNA noise figure, in dB, at ddm_timestamp_utc. Estimated from pre-launch characterization of LNA performance as a function of LNA temperature.
rx_to_sp_range	Rx to specular point range	int	meter	sample, ddm	The distance between the CYGNSS spacecraft and the specular point, in meters, at ddm_timestamp_utc.
tx_to_sp_range	Tx to specular point range	int	meter	sample, ddm	The distance between the GPS spacecraft and the specular point, in meters, at ddm_timestamp_utc.
tx_pos_x	GPS Tx position X	int	meter	sample, ddm	The X component of the GPS spacecraft WGS84 reference frame ECEF position, in meters, at ddm_timestamp_utc. Fill value is -99999999.
tx_pos_y	GPS Tx position Y	int	meter	sample, ddm	The Y component of the GPS spacecraft WGS84 reference frame ECEF position, in meters, at ddm_timestamp_utc. Fill value is -99999999.
tx_pos_z	GPS Tx position Z	int	meter	sample, ddm	The Z component of the GPS spacecraft WGS84 reference frame ECEF position, in meters, at ddm_timestamp_utc. Fill value is -99999999.
tx_vel_x	GPS Tx velocity X	int	meter s-1	sample, ddm	The X component of the GPS spacecraft WGS84 reference frame ECEF velocity in meters, at ddm_timestamp_utc
tx_vel_y	GPS Tx velocity Y	int	meter s-1	sample, ddm	The Y component of the GPS spacecraft WGS84 reference frame ECEF velocity in meters, at ddm_timestamp_utc
tx_vel_z	GPS Tx velocity Z	int	meter s-1	sample, ddm	The Z component of the GPS spacecraft WGS84 reference frame ECEF velocity in meters, at ddm_timestamp_utc



bb_nearest	Time to most recent black body reading	float	second	sample, ddm	The time between ddm_timestamp_utc and the ddm_timestamp_utc of the closest (in time) black body reading, in signed seconds. A positive value indicates that the black body reading occurred after ddm_timestamp_utc. A negative value indicates that the block body reading occurred before ddm_timestamp_utc.
fresnel_coeff	Fresnel power reflection coefficient at specular point	float	1	sample, ddm	The SQUARE of the left hand circularly polarized Fresnel electromagnetic voltage reflection coefficient at 1575 MHz for a smooth ocean surface at the specular point location and incidence angle. See UM document 148-0361 Fresnel Coefficient Calculation for more information.
ddm_nbrcs	Normalized BRCS	float	1	sample, ddm	Normalized BRCS over an interpolated 3 delay x 5 Doppler region around the precise inter-bin specular point location [2]. The specular point bin is in the top (least delay) row and the center Doppler column of the 3 x 5 box. This value is computed only over the ocean due to the high confidence in the ocean specular point location. For land NBRCS values use ddm_nbrcs_center and ddm_nbrcs_peak.
ddm_nbrcs_scale_factor	Normalized BRCS Scale Factor	float	1	sample, ddm	Scale factor applied to the ddm_nbrcs during the statistical de-biasing process. Computed as a function of FM, antenna, SVN, and incidence angle.
ddm_les	Leading edge slope	float	1	sample, ddm	Leading edge slope of a 3 delay x 5 Doppler bin box that include the specular point bin. The specular point bin is in the top (least delay) row and the center Doppler column of the 3 x 5 box.
nbrcs_scatter_area	NBRCS scattering area	float	meter ²	sample, ddm	The scattering area of the 3 x 5 region of the ddm used to calculate ddm_nbrcs.
les_scatter_area	LES scattering area	float	meter ²	sample, ddm	The scattering area of the 3 x 5 region of the ddm used to calculate ddm_les.
brcs_ddm_peak_bin_delay_row	BRCS DDM peak bin delay row	byte	1	sample, ddm	The zero-based delay row of the peak value in the bistatic radar cross section DDM (brcs). Ranges from 0 to 16.
brcs_ddm_peak_bin_dopp_col	BRCS DDM peak bin Doppler column	byte	1	sample, ddm	The zero-based Doppler column of the peak value in the bistatic radar cross section DDM (brcs). Ranges from 0 to 10.
brcs_ddm_sp_bin_delay_row	BRCS DDM specular point delay row	float	1	sample, ddm	The zero-based delay row of the specular point delay in the bistatic radar cross section DDM (brcs). Note that this is a floating point value.
brcs_ddm_sp_bin_dopp_col	BRCS DDM specular point Doppler column	float	1	sample, ddm	The zero-based Doppler column of the specular point Doppler in the bistatic radar cross section DDM (brcs). Note that this is a floating point value.
ddm_brcs_uncert	DDM BRCS	float	1	sample, ddm	Uncertainty of the BRCS.



ATBD Level 1B DDM Calibration

	uncertainty				
bb_power_temperature_density	Black Body Power Temperature Density	float	Counts/Kelvin	sample,ddm	Raw counts of detected power radiated by the blackbody calibration target, divided by receiver gain and blackbody physical temperature in Kelvins, gives the detected power per unit absolute temperature.
ddm_nadir_signal_correction	Nadir Signal Correction Factor	float	1	sample,ddm	The correction factor applied to signal value based on the nadir bin ratio.
ddm_nadir_bb_correction_prev	Nadir BB Correction Factor Previous	float	1	sample,ddm	The correction factor applied to the previous blackbody value based on the nadir bin ratio.
ddm_nadir_bb_correction_next	Nadir BB Correction Factor Next	float	1	sample,ddm	The correction factor applied to the next blackbody value based on the nadir bin ratio.
zenith_sig_i2q2	Zenith Signal I2Q2	int	1	sample,ddm	Raw counts of detected power in direct GPS L1 C/A signal received by zenith navigation antenna and detected by navigation receiver.
zenith_sig_i2q2_corrected	Zenith Signal I2Q2 Corrected	float	1	sample,ddm	The zenith_sig_i2q2 after a correction factor, based on the zenith antenna bin ratio, has been applied.
zenith_sig_i2q2_mult_correction	Zenith Signal I2Q2 Multiplicative Correction Factor	float	1	sample,ddm	The multiplicative correction factor applied with zenith_sig_i2q2_corrected = $10 \cdot \log_{10}(\text{zenith_sig_i2q2} \cdot \text{zenith_sig_i2q2_mult_correction}) - \text{zenith_sig_i2q2_add_correction}$.
zenith_sig_i2q2_add_correction	Zenith Signal I2Q2 Additive Correction Factor	float	1	sample,ddm	The additive correction factor applied with zenith_sig_i2q2_corrected = $10 \cdot \log_{10}(\text{zenith_sig_i2q2} \cdot \text{zenith_sig_i2q2_mult_correction}) - \text{zenith_sig_i2q2_add_correction}$.
starboard_gain_setting	The Nadir-Starboard Gain Setting	int	dB	sample,ddm	The Nadir-Starboard Gain Setting (dB, 0=Automatic)
port_gain_setting	The Nadir-Port Gain Setting	int	dB	sample,ddm	The Nadir-Port Gain Setting (dB, 0=Automatic)
ddm_kurtosis	DDM Kurtosis	float	1	sample,ddm	The kurtosis of the DDM noise floor. For diagnostic use only. See UM document 148-0347 DDM RFI Algorithm for more information.
modis_land_cover	MODIS Land Cover classification	byte	1	sample,ddm	The MODIS Land Cover Classification type at the specular point latitude and longitude
srtm_dem_alt	SRTM DEM altitude	float	meter	sample,ddm	Altitude at the specular point calculated using the 1km resolution SRTM DEM. Land observations only.
srtm_slope	SRTM DEM slope	float	degree	sample,ddm	Surface slope at the specular point calculated using the 1km resolution SRTM DEM. Land observations only.



reflectivity_peak	Peak linear reflectivity	float	linear	sample,ddm	Surface reflectivity calculate at the DDM peak power bin [3].
ddm_nbrcs_center	DDM NBRCS calculated around the central bin	float	1	sample,ddm	Approximation of the DDM NBRCS using a fixed and centered delay/Doppler grid in the BRCS DDM. Calculated by dividing the sum of a 3x5 grid of the BRCS DDM (brcs) by the sum of the equivalent grid from the effective scattering area DDM (eff_scatter). The grid region consists of 3 delay bins and 5 Doppler bins centered at delay bin 9 and Doppler bin 5 (using zero based indexing) of the BRCS and effective area DDMs. Computed only over land.
ddm_nbrcs_peak	DDM NBRCS calculated at the peak bin	float	1	sample,ddm	Approximation of the DDM NBRCS using the peak DDM only. Calculated by dividing the BRCS DDM peak bin (brcs) by the single central effective scatter area bin (eff_scatter). Computed only over land.
coherency_state	Coherency State	byte	1	sample,ddm	Meaning of each confidence state value: 0 = Not coherent 1 = Coherent 2 = Mixed Coherence 3 = Indeterminate Coherence
coherency_ratio	Coherency Ratio	float	1	sample,ddm	Estimation of the ratio of received power between the central bins and periphery bins of the raw_counts DDM after the elimination of noise bins [4]. A higher ratio is more indicative of signal coherence
sp_land_valid	Is land SP valid?	byte	1	sample,ddm	Land specular point location estimate is valid with reasonable confidence, as per the calculation algorithm described in [4]. This flag is set to 1 (valid) if the sp_land_confidence value is either 3 or 4, and set to 0 (invalid) otherwise.
sp_land_confidence	Confidence in land specular point	byte	1	sample,ddm	Meaning of each confidence value: 0 = Lowest confidence, land SP wrong 1 = Land SP probably wrong, but low SNR is the cause 2 = Land SP probably OK, despite low SNR 3 = Highest confidence, land SP OK
ddmi_tracker_delay_center	DDMI Tracker Delay Center	float	1	sample,ddm	The navigation receiver clock drift contribution to the received signal Doppler frequency. Estimated during the 1Hz DMR navigation velocity solution as receiver clock bias rate, converted to frequency (Hz).
rx_clk_doppler	Rx Clock Doppler	int	dB	sample,ddm	The navigation receiver clock drift contribution to the received signal Doppler frequency. Estimated during the 1Hz DMR navigation velocity solution as receiver clock bias rate, converted to frequency (Hz).



pekel_sp_water_percentage	Percentage of water at SP	byte	1	sample,ddm	The interpolated lookup of the percentage of water on a high resolution (30m) Pekel water mask.
pekel_sp_water_flag	Possible surface water at SP	byte	1	sample,ddm	If pekel_sp_water_percentage > 0, pekel_sp_water_flag = 1, else 0. Water presence estimated in the vicinity of the SP using high resolution (30m) Pekel water mask.
pekel_sp_water_percentage_2km	Percentage of water within 2km of SP	byte	1	sample,ddm	The percentage of water within a 2km circular region centered at the SP. Water presence estimated in the vicinity of the SP using high resolution (30m) Pekel water mask.
pekel_sp_water_flag_2km	Water estimated within 2km of SP	byte	1	sample,ddm	If pekel_sp_water_percentage_2km > 0, pekel_sp_water_flag_2km = 1, else 0. Water presence estimated in the vicinity of the SP using high resolution (30m) Pekel water mask.
pekel_sp_water_percentage_5km	Percentage of water within 5km of SP	byte	1	sample,ddm	The percentage of water within a 5km circular region centered at the SP. Water presence estimated in the vicinity of the SP using high resolution (30m) Pekel water mask.
pekel_sp_water_flag_5km	Water estimated within 5km of SP	byte	1	sample,ddm	If pekel_sp_water_percentage_5km > 0, pekel_sp_water_flag_5km = 1, else 0. Water presence estimated in the vicinity of the SP using high resolution (30m) Pekel water mask.
pekel_sp_water_percentage_10km	Percentage of water within 10km of SP	byte	1	sample,ddm	The percentage of water within a 10km circular region centered at the SP. Water presence estimated in the vicinity of the SP using high resolution (30m) Pekel water mask.
pekel_sp_water_flag_10km	Water estimated within 10km of SP	byte	1	sample,ddm	If pekel_sp_water_percentage_10km > 0, pekel_sp_water_flag_10km = 1, else 0. Water presence estimated in the vicinity of the SP using high resolution (30m) Pekel water mask.
pekel_sp_water_local_map_5km	Local area map of the water mask	byte	1	sample,ddm,lat_5km,lon_5km	A 5 km x 5 km local area grid of Pekel percentage of surface water. Each cell of the local area map is 1km x 1km. The reported sp_lat, sp_lon, and sp_land_alt is the center cell of the local area map.
sp_calc_method	Specular point calculation method	byte	1	sample,ddm	Method used for Specular Point Calculation: 0 = Ocean, uses DTU10 for altitude 1 = Land, uses SRTM for altitude
quality_flags	Per-DDM quality flags 1	int	<none>	sample, ddm	First group of the Per-DDM quality flags. 1 indicates presence of condition. More quality flags can be found in quality flags 2. Flag bit masks:



					<p>1/0x00000001 (Bit 01) = ocean_poor_overall_quality: Set if this sample is determined to be of overall poor quality for ocean applications. The logical OR of the following flags. If any one of the following flags are set then ocean_poor_overall_quality will be set: large_sc_attitude_err, black_body_ddm, ddmi_reconfigured, spacewire_crc_invalid, ddm_is_test_pattern, channel_idle, low_confidence_ddm_noise_floor, sp_over_land, sp_very_near_land, large_step_noise_floor, large_step_lna_temp, direct_signal_in_ddm, low_confidence_gps_eirp_estimate, rfi_detected, brcs_ddm_sp_bin_delay_error, brcs_sp_bin_dopp_error, gps_pvt_sp3_error, sp_non_existent_error, brcs_lut_range_error, ant_data_lut_range_error, bb_framing_error, fsw_comp_shift_error, sc_altitude_out_of_nominal_range, anomalous_sampling_period, invalid_roll_state, incorrect_ddmi_antenna_selection(quality_flags_2), sp_in_sidelobe(quality_flags_2), fatal_nst_outage(quality_flags_2), low_zenith_ant_gain(quality_flags_2), poor_bb_quality(quality_flags_2), low_coherency_ratio(quality_flags_2)</p>
					<p>2/0x00000002 (Bit 02) = s_band_powered_up: Set if S-band transmitter is powered up.</p>
					<p>4/0x00000004 (Bit 03) = small_sc_attitude_err: Set if the absolute value of the spacecraft roll is between 1 and 30 degrees, the pitch is between 1 and 10 degrees, or the yaw is between 1 and 5 degrees.</p>
					<p>8/0x00000008 (Bit 04) = large_sc_attitude_err: Set if the absolute value of the spacecraft roll is greater than or equal to 30 degrees, the pitch is greater than or equal to 10 degrees, or the yaw is greater than or equal to 5 degrees.</p>
					<p>16/0x00000010 (Bit 05) = black_body_ddm: Set if the black body load was selected during the DDM sampling period.</p>
					<p>32/0x00000020 (Bit 06) = ddmi_reconfigured: Set if the DDMI</p>



					was reconfigured during the DDM sampling period.
					64/0x00000040 (Bit 07) = spacewire_crc_invalid: Set if the DDM CRC transmitted from the DDMI to the spacecraft computer was not valid.
					128/0x00000080 (Bit 08) = ddm_is_test_pattern: Set if the DDM is a test pattern generated by the DDMI.
					256/0x00000100 (Bit 09) = channel_idle: Set if this reflectometry channel was not tracking a PRN.
					512/0x00000200 (Bit 10) = low_confidence_ddm_noise_floor: Set if the difference between this DDM noise floor and the previous DDM noise floor is greater than 10%.
					1024/0x00000400 (Bit 11) = sp_over_land: Set if the specular point is over land. Referenced using a map with 0.1 degree lat/lon bins. Coastline features or islands smaller than bin size may not be properly captured.
					2048/0x00000800 (Bit 12) = sp_very_near_land: Set if the specular point is within 25 km of land. Referenced using a map with 0.1 degree lat/lon bins.
					4096/0x00001000 (Bit 13) = sp_near_land: Set if the specular point is within 50 km of land. Referenced using a map with 0.1 degree lat/lon bins.
					8192/0x0002000 (Bit 14) = large_step_noise_floor: Set if the difference between this DDM noise floor and the previous DDM noise floor is greater than 0.24 dB.
					16384/0x00004000 (Bit 15) = large_step_lna_temp: Set if the LNA temperature rate of change is greater than 1 degree C per minute.
					32768/0x00008000 (Bit 16) = direct_signal_in_ddm: Set if the absolute value of the difference between direct signal code phase and the DDM signal code phase is less than or equal to four.
					65536/0x00010000 (Bit 17) = low_confidence_gps_eirp_estimate: Set when there is low confidence in the GPS effective isotropic radiated power estimate.
					131072/0x00020000 (Bit 18) = rfi_detected: Set when the kurtosis of the DDM noise floor deviates from pure Gaussian (3.0) by more than 1.0.



					262144/0x00040000 (Bit 19) = brcs_ddm_sp_bin_delay_error. Set if the calculated specular point bin zero-based delay row is greater than 4 (ocean) / 1 (land) and less than 8 (ocean) / 15 (land).
					524288/0x00080000 (Bit 20) = brcs_ddm_sp_bin_dopp_error. Set if the calculated specular point bin zero-based Doppler column is is greater than 4 (ocean) / 1 (land) and less than 6 (ocean) / 11 (land).
					1048576/0x00100000 (Bit 21) = neg_brcs_value_used_for_nbrcs. Set if any bin in the 3 x 5 brcs area used to calculate ddm_nbrcs has a negative value.
					2097152/0x00200000 (Bit 22) = gps_pvt_sp3_error. Cannot calculate GPS SV position/velocity/time from SP3 file.
					4194304/0x00400000 (Bit 23) = sp_non_existent_error. Specular point does not exist.
					8388608/0x00800000 (Bit 24) = brcs_lut_range_error. Unable to index into BRCS uncertainty lookup table.
					16777216/0x01000000 (Bit 25) = ant_data_lut_range_error. Unable to index into antenna data lookup table.
					33554432/0x02000000 (Bit 26) = bb_framing_error. Insufficient black body data for calibration.
					67108864/0x04000000 (Bit 27) = fsw_comp_shift_error. Flight software telemetry encoding error of the fsw_comp_delay_shift and fsw_comp_dopp_shift variables. Corrected in FSW version 4.5.
					134217728/0x08000000 (Bit 28) = low_quality_gps_ant_knowledge: Not enough data is available to properly calibrate the NBRCS for this sample's GPS satellite.
					268435456/0x10000000 (Bit 29) = sc_altitude_out_of_nominal_range: The spacecraft's altitude is out of nominal altitude range. Nominal altitude is defined as between 490 km to 550 km.
					536870912/0x20000000 (Bit 30) = anomalous_sampling_period: Set when an anomaly was observed on the CYGNSS or GPS satellite while this sample was taken. These samples have produced data that do not align with typical CYGNSS results. See up to date list at: https://docs.google.com/spreadsheets/d/1



					AFAZanVGDApLSnJQAAdPfOKoJQs 0jnB8ZvIuD1Z5mAc/edit?usp=sharing
					1073741824/0x40000000 (Bit 31) = invalid_roll_state: The spacecraft's reported roll angle is more than 1 degree from the commanded roll.
quality_flags_2	Per-DDM quality flags 2	int	<none>	sample, ddm	Second group of the Per-DDM quality flags. 1 indicates presence of condition. The first group of quality flags can be found in quality_flags. Flag bit masks:
					1/0x00000001 (Bit 01) = incorrect_ddmi_antenna_selection: The wrong (port or starboard) antenna was selected.
					2/0x00000002 (Bit 02) = high_signal_noise: The signal is in the highest noise group, but there are still some OK noise rows. Samples are suspect, but may contain quality data. Flag only used for land applications.
					4/0x00000004 (Bit 03) = noise_floor_cal_error: The signal is off or is very near the top rows of the full DDM. A proper noise floor cannot be computed. Flag only used for land applications.
					8/0x00000008 (Bit 04) = sp_in_sidelobe: The specular point is in the sidelobe causing low confidence in the antenna gain.
					16/0x00000010 (Bit 05) = negligible_nst_outage: Minor star track outage with negligible impact on attitude knowledge
					32/0x00000020 (Bit 06) = minor_nst_outage: Minor star track outage with small but acceptable impact on attitude knowledge
					64/0x00000040 (Bit 07) = fatal_nst_outage: Star track outage with unacceptable impact on attitude knowledge
					128/0x00000080 (Bit 08) = low_zenith_ant_gain: Zenith antenna gain is less than -6 dB
					256/0x00000100 (Bit 09) = poor_bb_quality: The distance between the surrounding BB samples > 1350 seconds OR the absolute value of the time to the nearest BB > 350 seconds.



					512/0x00000200 (Bit 10) = poor_quality_bin_ratio: Bin ratio on the nadir or zenith antenna is associated with degraded performance.
					1024/0x00000400 (Bit 11) = low_coherency_ratio: Indicates low confidence in coherence state given comparable signal power levels to the measurement's noise floor.
					2048/0x00000800 (Bit 12) = land_poor_overall_quality: Set if this sample is determined to be of overall poor quality for land applications. The logical OR of the following flags. If any one of the following flags are set then land_poor_overall_quality will be set: large_sc_attitude_err, black_body_ddm, ddmi_reconfigured, spacewire_crc_invalid, ddm_is_test_pattern, channel_idle, large_step_lna_temp, direct_signal_in_ddm, low_confidence_gps_eirp_estimate, gps_pvt_sp3_error, sp_non_existent_error, ant_data_lut_range_error, bb_framing_error, fsw_comp_shift_error, sc_altitude_out_of_nominal_range, anomalous_sampling_period, invalid_roll_state, incorrect_ddmi_antenna_selection(quality_flags_2), noise_floor_cal_error(quality_flags_2), sp_in_sidelobe(quality_flags_2), fatal_nst_outage(quality_flags_2), low_zenith_ant_gain(quality_flags_2), poor_bb_quality(quality_flags_2), sp_over_ocean(quality_flags_2), sp_extremely_near_ocean(quality_flags_2), land_obs_range_error(quality_flags_2)
					4096/0x00001000 (Bit 13) = sp_over_ocean: Set if the specular point is over ocean. Referenced using a map with 0.1 degree lat/lon bins. Coastline features or islands smaller than bin size may not be properly captured.
					8192/0x00002000 (Bit 14) = sp_extremely_near_ocean: Set if the specular point is within 10 km of ocean. Referenced using a map with 0.1 degree lat/lon bins.
					16384/0x00004000 (Bit 15) = sp_very_near_ocean: Set if the specular point is within 25 km of ocean. Referenced using a map with 0.1 degree lat/lon bins.



					32768/0x00008000 (Bit 16) = land_obs_range_error: Set if any value in an L1 land observable calculation is outside of the valid range. This flag is currently set if the sum of the effective scattering area is 0 when computing ddm_nbrcs_peak or ddms_nbrcs_center
Per-Bin Values					
raw_counts	DDM bin raw counts	int	1	sample, ddm, delay, doppler	17 x 11 array of DDM bin raw counts. These are the uncalibrated power values produced by the DDMI.
power_analog	DDM bin analog power	float	watt	sample, ddm, delay, doppler	17 x 11 array of DDM bin analog power, Watts. analog_power is the true power that would have been measured by an ideal (analog) power sensor. power_digital is the power measured by the actual 2-bit sensor, which includes quantization effects. power_analog has been corrected for quantization effects.
brcs	DDM bin bistatic radar cross section	float	meter ²	sample, ddm, delay, doppler	17 x 11 array of DDM bin bistatic radar cross section, m ² . The specular point is located in DDM bin round(brcs_ddm_sp_bin_delay_row), round(brcs_ddm_sp_bin_dopp_col).
eff_scatter	DDM bin effective scattering area	float	meter ²	sample, ddm, delay, doppler	17 x 11 array of DDM bin effective scattering area, m ² . This is an estimate of the true surface scattering area that contributes power to each DDM bin, after accounting for the GPS signal spreading function. It is calculated by convolving the GPS ambiguity function with the surface area that contributes power to a given DDM bin as determined by its delay and Doppler values and the measurement geometry. The specular point bin location matches the specular point bin location in brcs.